Shock Wave Boundary Layer Interactions
in High Mach Number Flows
A Critical Survey of Current Numerical Prediction Capabilities

Doyle D. Knight
Department of Mechanical and Aerospace Engineering
Rutgers – The State University of New Jersey
98 Brett Road, Piscataway NJ 08854-8059
USA

Gérard Degrez
Aerospace Department
von Karman Institute for Fluid Dynamics
Chaussée de Waterloo, 72 – B-1640 Rhode-Saint-Genèse
Belgium

Abstract

The report assesses the capability for numerical simulation of 2-D and 3-D shock wave laminar and turbulent boundary layer interactions. Three fundamental configurations are considered: single fin, double fin, and hollow cylinder flare. Thirteen separate cases were examined by a distinguished international group of researchers using the Reynolds-averaged Navier-Stokes (RANS) equations with a wide range of turbulence models from zero equation to full Reynolds Stress Equation formulations. The report presents an extensive comparison of computations and experimental data, summarizes the results, and makes recommendations for future research.

1 Introduction

The interaction between shock waves and boundary layers is a common occurrence in aerodynamics and aeropropulsion. Examples include deflection of control surfaces, high speed inlets, rotorcraft, transonic compressors, and wing- and tail-fuselage junctures. The interactions can significantly affect the performance of aeronautical systems. For example, the interaction on a deflected control surface can cause significant changes in the surface pressure and hence control moments.

Numerous reviews have been published on shock wave boundary layer interaction. Examples include Greene [1], Korkegi [2], Peake and Tobak [3], Delery and Marvin [4], Settles and Dolling [5, 6], Stollery [7], Degrez et al. [8], Delery and Panaras [9], and Zheltovodov [10].

The objective of this paper is to assess the capability for simulation of 2-D and 3-D shock wave boundary layer interactions. A test matrix of configurations (Table 1), based on the report of Delery and Panaras [9], was established. An international group of researchers (Table 2) participated in computation of one or more of the cases by using a variety of turbulence models. The results are presented in this paper, and conclusions are drawn for future work.

Table 1: Test Matrix

Configuration	Type	No. Cases
Single fin	Turbulent	7
Double fin	Turbulent	4
Hollow cylinder flare	Laminar	1
Hollow cylinder flare	Turbulent	1

The details of the numerical algorithms, turbulence models and grids are presented in the individual references of the participants. The computations were conducted in a careful manner

to ensure accurate results. In many instances, grid refinement studies were performed to firmly establish the uncertainties in the numerical solutions. The reader is referred to the individual participants for further information regarding the numerical methodology.

Table 2: Participants

Participant	Organization
Greg Alexopoulos	North Carolina State Univ
J.-M. Bousquet	ONERA
R. Bur	ONERA
Gérard Degrez	Von Karman Institute
Jack Edwards	North Carolina State Univ
Datta Gaitonde	Wright Labs, WPAFB, OH
Marianna Gnedin	Rutgers University
F. Grasso	Università di Roma
Hassan Hassan	North Carolina State Univ
C. C. Horstman	NASA Ames
Doyle Knight	Rutgers University
James Moss	NASA Langley
Natraj Narayanswami	Rutgers University
Argyris Panaras	Hellenic AF Academy
Patrick Rodi	Univ of Texas-Austin
Balu Sekar	Wright Labs, WPAFB, OH
Edwin Van der Weide	Von Karman Institute
Gecheng Zha	Rutgers University

2 Single Fin

The single fin geometry is a wedge of angle α attached normal to a flat plate (Fig. 1) on which an equilibrium turbulent boundary layer has developed. The wedge generates an oblique shock wave which interacts with the boundary layer on the flat plate. The flow parameters are the Mach number M_∞, Reynolds number Re_{δ_∞} based on the upstream boundary layer thickness δ_∞, fin angle α, and wall temperature ratio T_w/T_∞. The fin is assumed to be semi-infinite in height and length.

The flowfield structure of the single fin interaction is generally understood. Detailed descriptions are presented in Alvi and Settles [11] and Zheltovodov and Shilein [12]. Provided that the shock strength is sufficient to cause separation, the wave structure and mean streamline pattern are approximately conical (see, for example, [13, 11]). Conical flow is defined in Appendix A. Thus, for example, the surface pressure and sur-
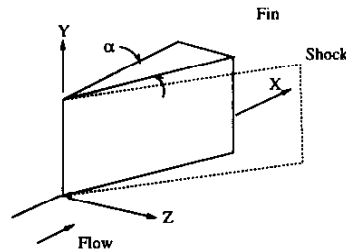

Figure 1: Single fin geometry

face flow visualization display conical behavior outside of an "inception zone" near the fin. An example (from [11]) is shown in Fig. 2 corresponding to case SF4 of this study. The wave structure includes a bifurcated shock (λ-shock) and slip line. The boundary layer separates to form a vortex whose center is approximately beneath the primary inviscid shock. Additional features may appear, depending on the shock strength including secondary separation of the boundary layer beneath the vortex, a normal shock in the impinging jet which turns back over the vortex, and supersonic reversed flow. Further discussion of these features is presented, for example, in Alvi and Settles [11], Zheltovodov et al [14] and Zubin and Ostapenko [15]. Other aspects of the single fin interaction flowfield do not display conical behavior, e.g., the surface heat transfer [16]. Overall, therefore, the single fin interaction can be viewed as quasi-conical.
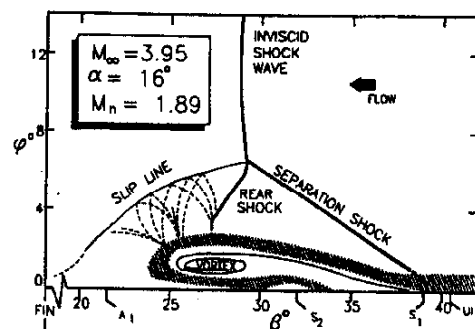

Figure 2: Flowfield structure (Case SF4) [11]

Seven configurations were computed by one or more of the participants. The flow conditions are shown in Table 3. The cases are ordered by the value of the normal Mach number M_n which determines the shock strength according to

$$\frac{p_2}{p_1} = \frac{2\gamma M_n^2 - (\gamma-1)}{\gamma+1} \tag{1}$$

There were five participants in the single fin studies (Table 4). Eleven computations employed the RANS equations, and two used the conical RANS equations. The turbulence models employed are shown in Table 5.

Table 3: Single Fin Cases

Case	Ref	M_n	M_∞	α	Re_{δ_∞} $(\times 10^5)$	T_w/T_{aw}
SF1	[16]	1.50	4.9	8°	2.3	0.80
SF2	[17]	1.65	3.0	16°	1.9	1.06
SF3	[18]	1.82	2.9	20°	8.1	1.00
SF4	[17]	1.89	4.0	16°	2.1	1.06
SF5	[16]	2.12	4.9	16°	2.3	0.80
SF6	[17]	2.14	4.0	20°	2.1	1.06
SF7	[19]	2.90	8.2	15°	1.8	0.28

Note: Most experimental data tabulated in [20].

LEGEND

M_n	$M_\infty \sin\theta$	M_∞	Mach number
α	Fin angle	T_w	Wall temperature
θ	Shock angle	T_{aw}	Adiabatic T_w
Re_{δ_∞}	$\rho_\infty U_\infty \delta_\infty/\mu_\infty$		

Table 4: Participants for Single Fin Cases

Participant/SF	1	2	3	4	5	6	7
Jack Edwards						•	•
C. C. Horstman			•	•		•	
Doyle Knight			•	•		•	
Argyris Panaras		•		•		•	
Patrick Rodi	★					★	

LEGEND

• RANS   ★ Conical RANS

2.1 Case SF1

The computations solved the conical form of the Navier-Stokes equations using the Baldwin-Lomax turbulence model. A grid refinement study was performed using three separate grids which yielded a grid independent solution. Computations using conical Navier-Stokes equations must be viewed with some skepticism. As indicated previously, the surface pressure exhibits conical behavior, while the surface heat transfer does not.

Table 5: Turbulence Models for Single Fin

Participant	Model	Ref
J. Edwards	Spalart-Allmaras-Edwards	[21]
C. C. Horstman	$k - \epsilon$	[22]
D. Knight	Baldwin-Lomax	[23]
A. Panaras	Baldwin-Lomax-Panaras	[24]
P. Rodi	Baldwin-Lomax	[23]

The surface pressure is shown in Fig. 3. The abscissa is β (see Appendix A) measured from the virtual conical origin [16], and the ordinate is the wall pressure normalized by the freestream static pressure. There is general agreement. However, the computations underestimate the location of the beginning of the pressure rise which is typical for the Baldwin-Lomax model [25]. No experimental data are close to the fin, and therefore comparison of the computed and experimental results for the location and level of the maximum pressure is not possible [16].
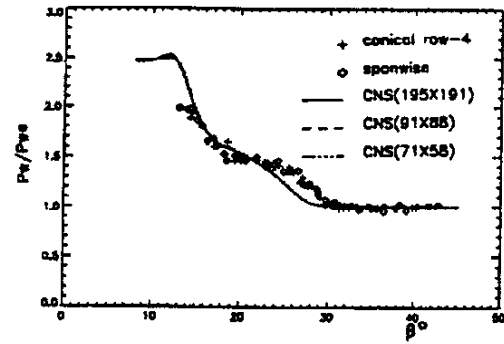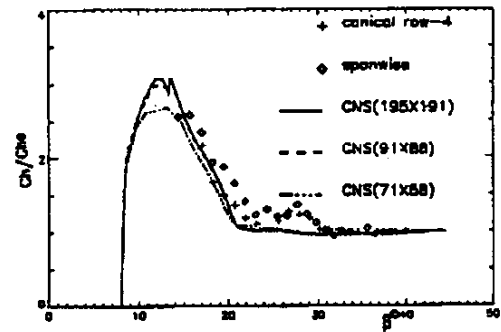

Figure 3: Surface pressure (Case SF1)

Figure 4: Heat transfer (Case SF1)

The heat transfer is shown in Fig. 4. The abscissa is β, and the ordinate is the heat transfer

coefficient normalized by its value immediately outside the interaction. Reasonable agreement is observed, except in the vicinity of the initial pressure rise ($\beta \approx 30°$). However, as noted previously, the experimental heat transfer does not behave in a conical manner, and thus the agreement may be somewhat fortuitous.

2.2 Case SF2

The surface pressure is shown in Fig. 5. The agreement between the Baldwin-Lomax-Panaras model and experiment is very good. The computation predicts both the plateau pressure, associated with the primary vortex (Fig. 2), and the peak pressure near the fin within 8%. The location of the beginning of the pressure rise is slightly underestimated.

The surface streamline angle Φ on the flat plate, measured relative to the freestream direction x, is displayed in Fig. 6. The ordinate is $\Phi - \beta$ in order to identify the separation and attachment lines which correspond to $\Phi - \beta = 0$. Good agreement is observed between the computation and experiment. The location of the primary separation line ($\beta = 45°$), secondary (incipient) separation line ($\beta = 37°$) and primary attachment line ($\beta = 21°$) are accurately predicted.

The skin friction coefficient c_f on the flat plate is shown in Fig. 7. The agreement is generally good. The computed skin friction displays a peak at $\beta = 25°$ which is not evident in the experiment. However, the number of experimental data points in this region is small, and thus a conclusive judgment on the accuracy of the c_f predictions cannot be made. For further discussion, see Panaras [24]. Minor discrepancies appear in the vicinity of the primary separation line at $\beta = 45°$.

2.3 Case SF3

The surface pressure at a fixed spanwise location $z/\delta_\infty = 6.8$ are shown in Fig. 8. The agreement is very good. There is very little difference between the predictions using the Baldwin-Lomax ("Theory-Knight") and $k - \epsilon$ ("Theory-Horstman") models.

The locations of selected streamwise stations for comparison of computed and experimental pitot
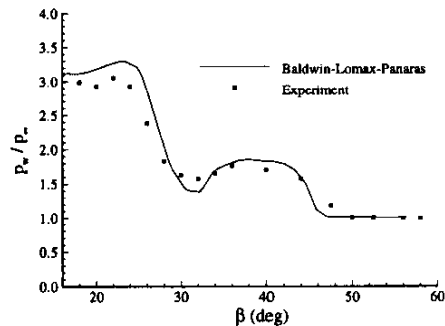
Figure 5: Surface pressure (Case SF2)
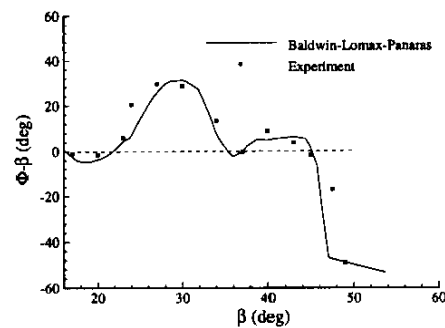
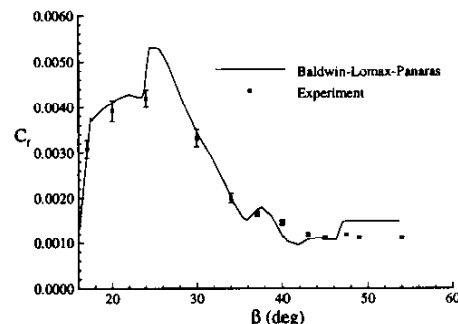Figure 6: Surface streamline angle (Case SF2)

Figure 7: Skin friction coefficient (Case SF2)

pressure and yaw angle are shown in Fig. 9. The yaw angle is defined as $\tan^{-1}(w/u)$ where u and w are the mean velocity components in the $x-$ and $z-$ directions, respectively. Location 5 is downstream of the separation line (line of coalescence) and upstream of the inviscid shock. Location 7 is close to the inviscid shock. Location 8 is downstream of the inviscid shock. Pitot pressure profiles are displayed in Figs. 10 to 12. The agreement is good[1]. In particular, the pitot pressure deficit associated with the primary vortex (at $y/\delta_\infty = 0.5$ in Fig. 11) is accurately predicted. Yaw angle profiles are shown in Figs. 13 to 15. Close agreement is again observed, except in the immediate vicinity of the surface (at $y/\delta_\infty < 0.5$ in Fig. 14). Overall, there are small differences between the predictions using the Baldwin-Lomax and $k-\epsilon$ models.

Figure 10: Pitot pressure at station 5 (Case SF3)

Figure 8: Surface pressure (Case SF3)
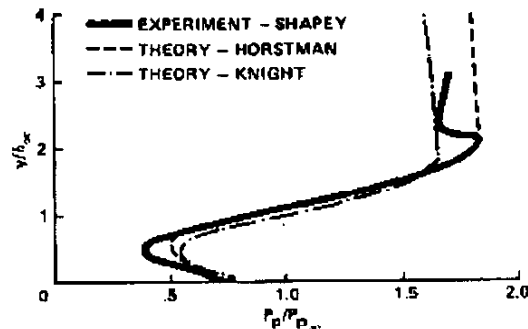
Figure 11: Pitot pressure at station 7(Case SF3)

Figure 9: Location of surveys (Case SF3)

[1]The region $y/\delta_\infty > 2$ in Fig. 11 is within the computed inviscid shock which is diffused over two to three grid cells, and therefore the differences in computed freestream pitot pressures are not significant.
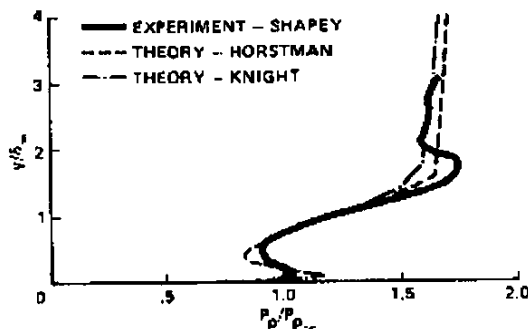
Figure 12: Pitot pressure at station 8 (Case SF3)
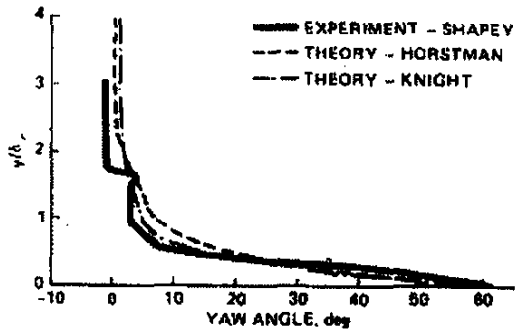
Figure 13: Yaw angle at station 5 (Case SF3)
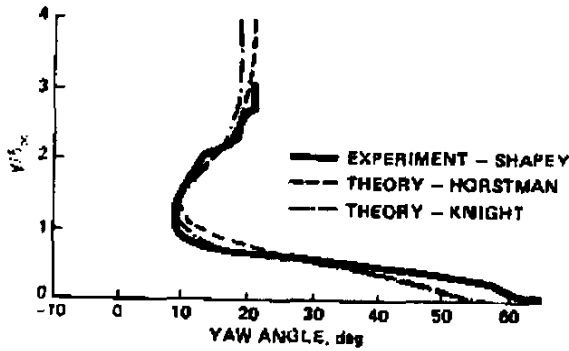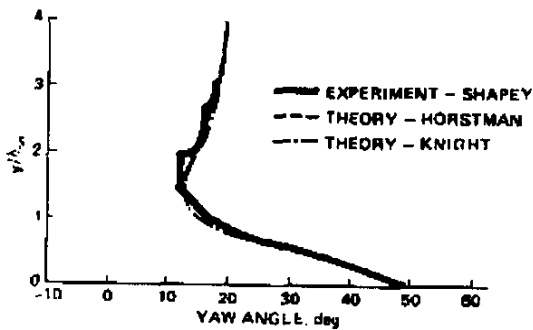

Figure 14: Yaw angle at station 7(Case SF3)

Figure 15: Yaw angle at station 8 (Case SF3)

2.4 Case SF4

The surface pressure is shown in Fig. 16. The Baldwin-Lomax-Panaras model is the most accurate. It predicts the plateau pressure within 5%, and the pressure trough (at $\beta = 27°$) within 13%. However, the peak pressure in the vicinity of the corner is overpredicted by 9%. The Baldwin-Lomax model underestimates slightly the location of the beginning of the pressure rise and fails to predict the pressure trough. However, it predicts the peak pressure at the corner within 4%. The $k-\epsilon$ model is the least accurate.
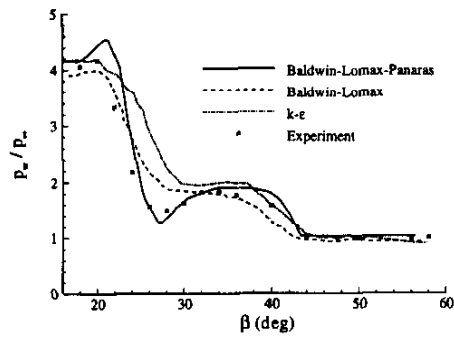
Figure 16: Surface pressure (Case SF4)

The surface streamline angle on the flat plate is displayed in Fig. 17. The ordinate is $\Phi - \beta$. The Baldwin-Lomax-Panaras is again the most accurate. It predicts the primary separation angle ($\beta = 41°$) within 4%, and the (incipient) secondary separation ($\beta = 33°$) within 9%. The Baldwin-Lomax and $k-\epsilon$ models also predict the primary angle within 4%; however, both fail to predict the secondary separation.
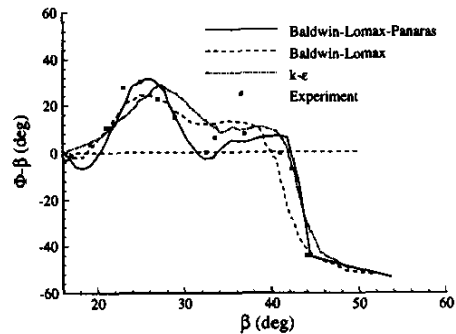
Figure 17: Surface streamline angle (Case SF4)

The skin friction coefficient is displayed in Fig. 18. The Baldwin-Lomax-Panaras model is more accurate, generally providing accurate prediction over the entire range of the interaction. The Baldwin-Lomax and k–ϵ models display the general trends of the experiment, but underestimate the peak skin friction by 30% to 35%.
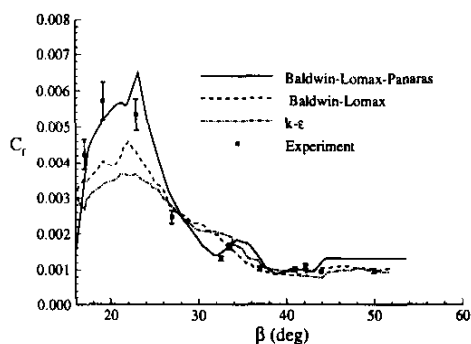

Figure 18: Skin friction coefficient (Case SF4)

2.5 Case SF5

The surface pressure is shown in Fig. 19. There is general agreement between the predictions using the Baldwin-Lomax model and the experiment. However, as observed in Case SF1, the computation underestimates the location of the beginning of the pressure rise. Since there are no experimental data close to the fin, comparison of the computed and experimental results for the location and level of the maximum pressure is not possible [16].
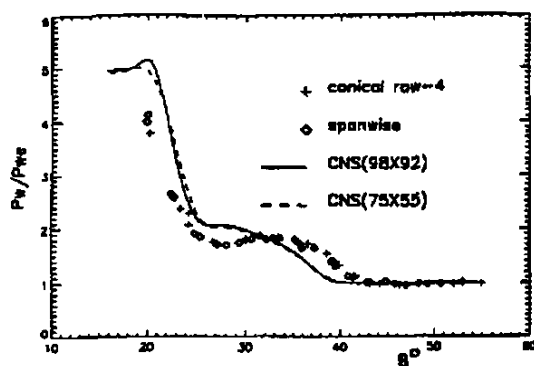
Figure 19: Surface pressure (Case SF5)

The heat transfer is shown in Fig. 20. Reasonable agreement is again observed, similar to Case SF1, except in the vicinity of the initial

pressure rise ($\beta \approx 40°$). However, the experimental heat transfer does not behave in a conical manner, and thus the good agreement may be fortuitous.
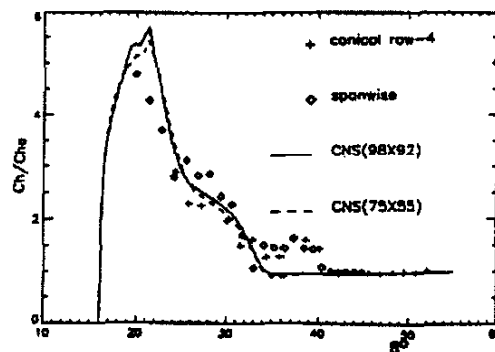

Figure 20: Heat transfer (Case SF5)

2.6 Case SF6

The surface pressure is shown in Fig. 21. The Baldwin-Lomax-Panaras and Spalart-Allmaras-Edwards models are the most accurate. Both models predict the surface pressure in the plateau region ($36° \le \beta \le 47°$) within 5% to 10%. Also, both models display a pressure trough at $\beta = 32°$, in agreement with the experiment, although the predictions differ from the experimental value by 30%. Both models overestimate the peak pressure in the vicinity of the corner by 11%. The predictions of the Baldwin-Lomax and k–ϵ models exhibit the general trends of the experiment but are less accurate.
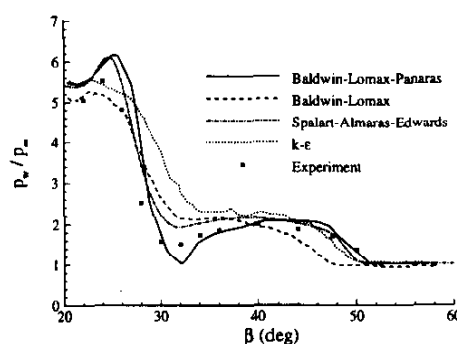

Figure 21: Surface pressure (Case SF6)

The surface streamline angle on the flat plate is displayed in Fig. 22. The Baldwin-

Lomax-Panaras is again the most accurate, with the Spalart-Allmaras-Edwards model providing nearly comparable results. The principal difference between the two predictions is in the region of the secondary separation at $\beta = 40°$. Again, the Baldwin-Lomax and $k - \epsilon$ models show general agreement with experiment, but are less accurate.
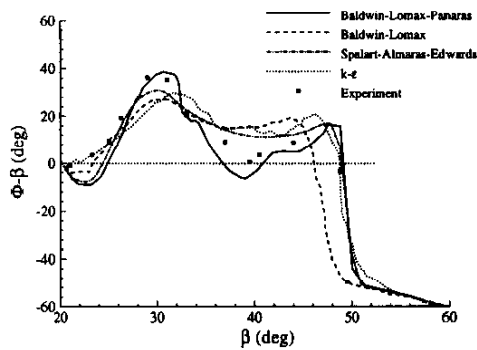

Figure 22: Surface streamline angle (Case SF6)

The skin friction coefficient is displayed in Fig. 23. The Baldwin-Lomax-Panaras and Spalart-Allmaras-Edwards models predict a peak in the vicinity of the corner which is not evident in the experiment[2]; in particular, their computed values at the experimental location $\beta = 26.5°$ are substantially above the experiment. Additional measurements in the region $22° < \beta < 26°$ would be helpful in determining whether a peak appears[3]. Elsewhere, all four models provide generally good agreement with the experiment.
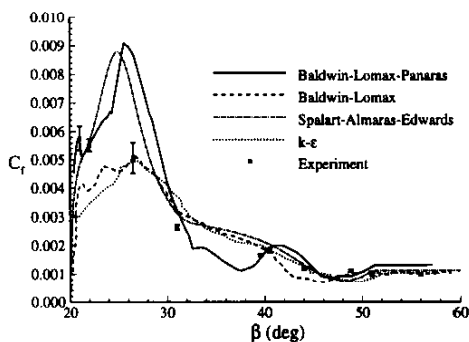
Figure 23: Skin friction coefficient (Case SF6)

---

[2] Corrected data for $\beta = 22°$ and $26.5°$, provided by Prof. G. Settles, is included in Fig. 23.

[3] Note that the attachment line is $\beta = 26°$ [11].

2.7 Case SF7

The surface pressure on the flat plate at $x/\delta_\infty = 4.9$ is displayed in Fig. 24. The agreement is very good. The Spalart-Allmaras-Edwards model provides an accurate prediction of the pressure distribution over the entire region. The peak pressure in the corner is predicted within 10%. The surface pressure on the fin at $x/\delta_\infty = 4.8$ is shown in Fig. 25. Similar close agreement is observed.
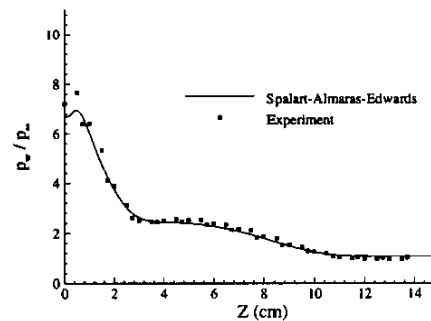

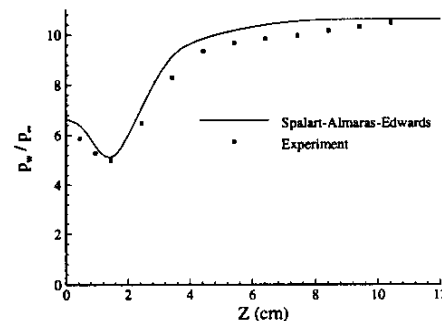Figure 24: Surface pressure on plate (Case SF7)

Figure 25: Surface pressure on fin (Case SF7)

The skin friction coefficient c_f is presented in Fig. 26. The agreement is very good. The peak c_f in the vicinity of the corner is predicted within the experimental uncertainty.

The heat transfer Q_w, normalized by the corresponding value in the upstream boundary layer Q_∞, is displayed in Figs. 27 and 28 for the flat plate and fin surfaces, respectively, at $x/\delta_\infty = 4.4$. The agreement is reasonably good. On the flat plate, the peak heat transfer in the vicinity of the corner is overpredicted by 35%, and underestimated in the plateau region typically
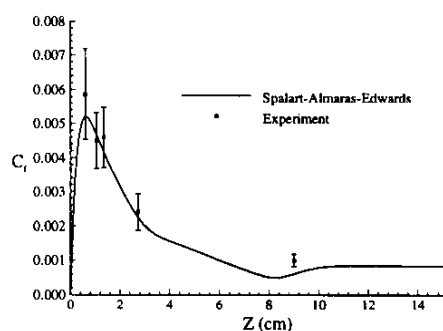
Figure 26: Skin friction on plate (Case SF7)

by 30%. A significant difference is evident on the fin surface away from the corner which is attributable to the assumption of fully turbulent flow from the leading edge in the computation. In the experiment, the boundary layer at this location and outside of the corner interaction was laminar.
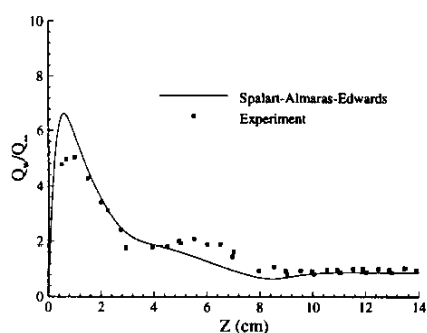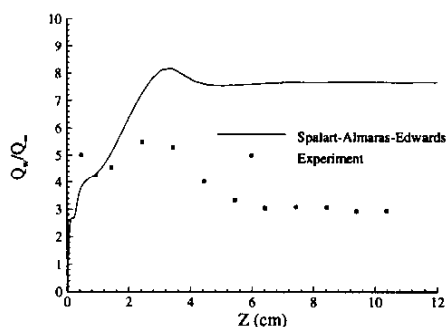

Figure 27: Heat transfer on plate (Case SF7)

Figure 28: Heat transfer on fin (Case SF7)

3 Double Fin

The double fin ("crossing shock") geometry consists of two wedges of angles α_1 and α_2 affixed normal to a flat plate (Fig. 29) on which an equilibrium turbulent boundary layer has developed. The wedges generate intersecting oblique shock waves which interact with the boundary layers on the flat plate and inner fin surfaces. The flow parameters are the Mach number M_∞, Reynolds number Re_{δ_∞}, fin angles α_1 and α_2, contraction ratio L_2/L_1, throat middle line offset L_3/L_1, boundary layer to throat width ratio δ_∞/L_2, and wall temperature ratio T_w/T_{aw}. The fins are assumed semi-infinite in height. For the symmetric double fin, $L_3 = 0$.
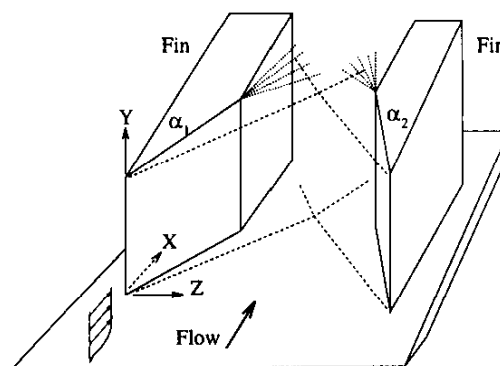

Figure 29: Double fin geometry

The flowfield structure of the double fin interaction is only partially understood. The interaction of the incident λ-shocks, generated by the initial single fin interactions, forms a complex wave system which is described in [26, 27, 28, 29, 30, 31] for the symmetric case, and in [32] for the asymmetric case. The principal mean streamline structure is a pair of counter-rotating vortices, generated by the initial single fin interactions, which merge to form a vortex pair which is associated with a region of low total pressure. A detailed discussion of the streamline structure for the symmetric case is presented in [33, 34, 35, 26, 27, 28] and for an asymmetric case in [32]. An example is shown in Fig. 30.

Four configurations were computed by one or more of the participants. The flow conditions are shown in Table 6. The cases are ordered in terms of magnitude of the pressure rise[4] p_4/p_1

---

[4]This particular choice of ordering, though obvious, is arbitrary. Unlike the single fin configuration, no param-
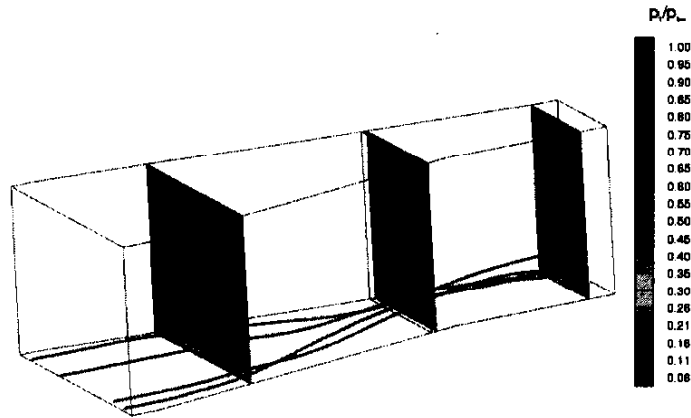
Figure 30: Computed streamlines and total pressure contours (Case DF2) using $k-\epsilon$ Chien model

Table 6: Double Fin Cases

Case	Ref	p_4/p_1	M_∞	α_1	α_2	Re_{δ_∞} $(\times 10^5)$	L_2/L_1	L_3/L_1	δ_∞/L_2	T_w/T_{aw}
DF1	[36]	3.4	4.0	7°	7°	3.1	0.45	0	0.11	1.11
DF2	[36]	4.6	4.0	7°	11°	3.0	0.44	0.014	0.11	1.11
DF3	[37]	10.2	3.9	15°	15°	2.6	0.32	0	0.11	1.06
DF4	[38]	45.0	8.3	15°	15°	1.6	0.28	0	0.75	0.28

LEGEND

M_∞	Freestream Mach number	α_1, α_2	Fin angles
Re_{δ_∞}	$\rho_\infty U_\infty \delta_\infty / \mu_\infty$	L_1	Distance between fins at entrance
L_2	Distance between fins at throat	L_3	Offset of TML
TML	Throat Middle Line	T_w	Wall temperature
T_{aw}	Adiabatic wall temperature		

across the intersecting shocks.

There were eleven participants in the double fin studies (Table 7). All computations employed the Reynolds-averaged compressible Navier-Stokes equations. The turbulence models employed are shown in Table 8.

Table 7: Participants for Double Fin Cases

Participant/DF	1	2	3	4
Jack Edwards		●	●	●
Datta Gaitonde			●	●
Mariana Gnedin	●	●		
Hassan Hassan & Greg Alexopoulos		●		●
C. C. Horstman				●
Doyle Knight		●		
Natraj Narayanswami			●	●
Argyris Panaras			●	
Balu Sekar		●		●
GeCheng Zha		●		

3.1 Case DF1

The computed skin friction lines using the $k - \epsilon$ Knight model and experimental surface flow visualization are shown in Figs. 31 and 32. The incident separation lines 1 and 2 which originate at the fin leading edges are visible. The computed and experimental separation line angles agree within 7%. The computed skin friction lines do not intersect. Rather, the lines slowly converge towards each other. Two weak divergence lines 3 and 4 are evident near the fin surfaces.

The surface pressure is shown in Figs. 33 and 34 along the Throat Middle Line[5] (TML) and at the three streamwise locations. The accuracy of the surface pressure measurements is ±0.5%. The computed surface pressure displays excellent agreement with experiment.

The surface heat transfer coefficient c_h is displayed in Figs. 35 to 38. The accuracy of the measurements is ±10% to ±15%. Reasonable

---

eter(s) have been demonstrated to appropriately categorize the double fin configuration.

[5]The Throat Middle Line is the streamwise plane which bisects the throat (i.e., the region of minimum cross section).

Table 8: Turbulence Models for Double Fin

Participant	Model	Ref
J. Edwards	Spalart-Allmaras-Edwards	[21]
D. Gaitonde	Baldwin-Lomax (BI,IB)	[26]
	$k - \epsilon$	[28]
	$k - \epsilon$ (CC)	[27, 2:
	$k - \epsilon$ (VC)	[28]
	$k - \epsilon$ (RH)	[28]
M. Gnedin	$k - \epsilon$ Knight	[39]
H. Hassan	$k - \omega$	[40]
C. C. Horstman	$k - \epsilon$ Rodi	[35]
D. Knight	$k - \epsilon$ Chien	[41]
N. Narayanswami	Baldwin-Lomax	[23]
A. Panaras	Baldwin-Lomax-Panaras	[24]
B. Sekar	Baldwin-Lomax	[42]
G. Zha	Reynolds Stress Equation	[43]

LEGEND

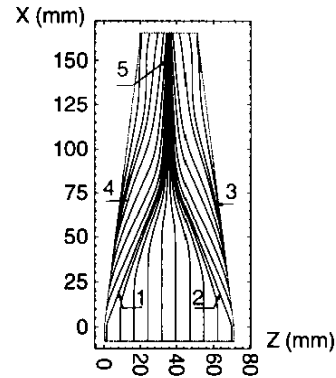|	
BI	Buleev Integral
CC	Compressibility correction
IB	Inverse blending
RH	Rodi-Horstman length scale modification
VC	Vuong-Coakley length scale modification

Figure 31: Computed skin friction lines (Case DF1):
1 Left incident separation line
2 Right incident separation line
3, 4 Lines of divergence
5 Downstream coalescence line

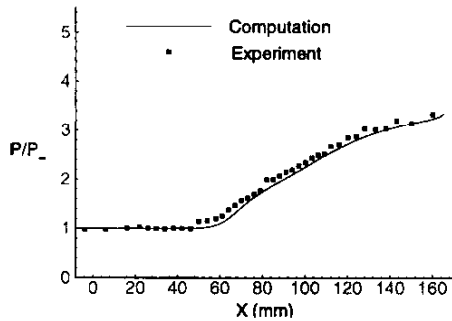Figure 32: Experimental surface flow (Case DF1)

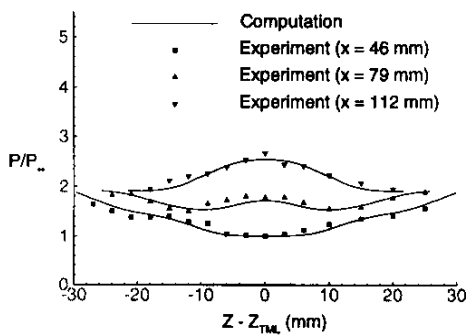Figure 33: Wall pressure on TML (Case DF1)

Figure 34: Wall pressure at $x = 46$ mm, $x = 79$ mm and $x = 112$ mm (Case DF1)

agreement with the experiment is observed. On the TML, the heat transfer coefficient is predicted typically within 25% in the 3-D interaction region.
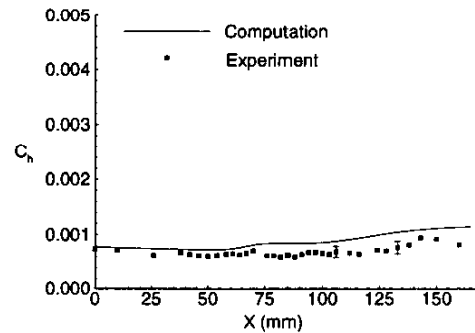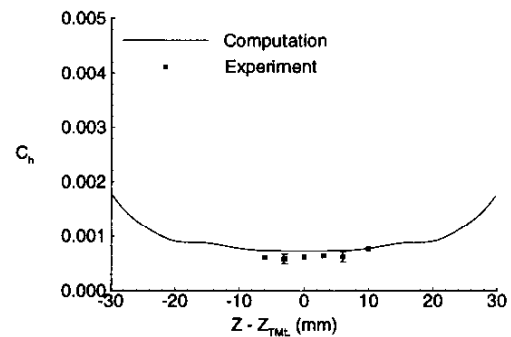

Figure 35: C_h on TML (Case DF1)
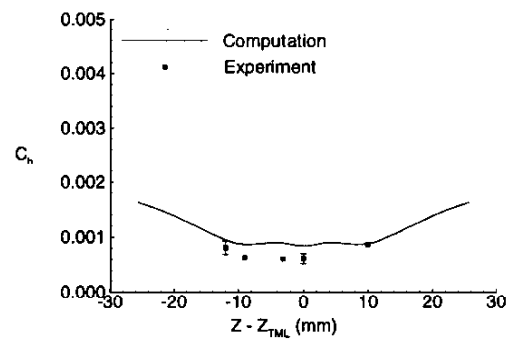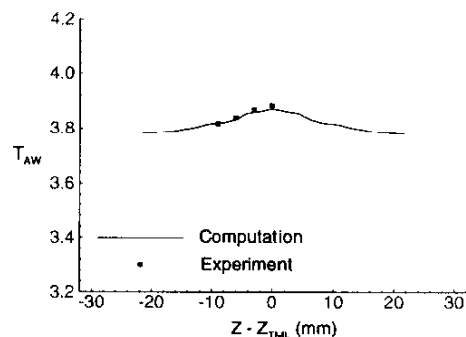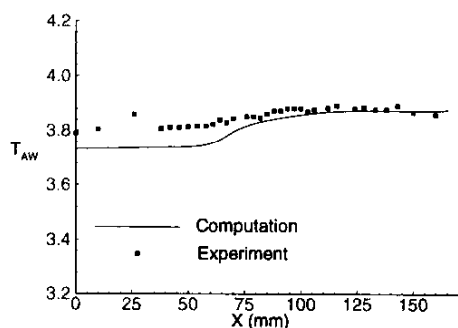

Figure 36: C_h at $x = 46$ mm (Case DF1)

Figure 37: C_h at $x = 79$ mm (Case DF1)

The adiabatic wall temperature T_{aw}/T_∞ is displayed in Figs. 39 to 42. The accuracy of the measurements is less than 0.2%. Close agreement is observed. The maximum difference between the predicted and measured T_{aw} is less than 2%.
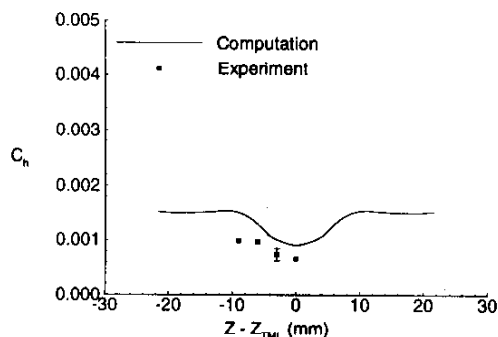
Figure 38: C_h at $x = 112$ mm (Case DF1)

Figure 39: T_{aw} on TML (Case DF1)
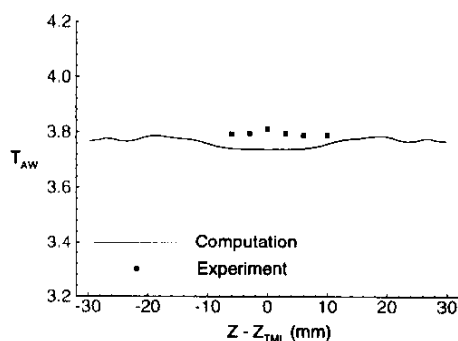
Figure 40: T_{aw} at $x = 46$ mm (Case DF1)
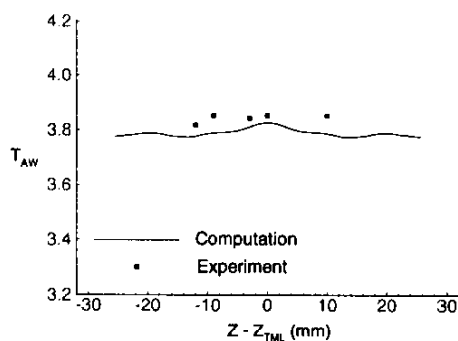
Figure 41: T_{aw} at $x = 79$ mm (Case DF1)

Figure 42: T_{aw} at $x = 112$ mm (Case DF1)

3.2 Case DF2

The computed surface skin friction lines using the $k-\epsilon$ Chien model and $k-\epsilon$ Knight model are shown in Figs. 43 and 44, respectively, and the experimental surface visualization is shown in Fig. 45. The incident separation lines emanating from the fin leading edges (1 and 2) are evident in both computations and experiment. The computed separation line angles, measured relative to the x-axis, agree with the experiment to within 10% for the $k-\epsilon$ Chien model and to within 9% for the $k-\epsilon$ Knight model. The $k-\epsilon$ Chien results display a coalescence of the incident separation lines into a narrow band (3) offset to the left side, in agreement with the experiment. This line represents the surface image of the boundary between the left and right vortices generated by the incident single fin interactions. The $k-\epsilon$ Chien results also show a second line of coalescence form alongside on the right and farther downstream (4) associated with a secondary separation underneath the left side of the right vortex [32], and a line of divergence alongside the right fin (5). A similar line of divergence (unmarked) is near the left fin.

For the $k-\epsilon$ Knight model (Fig. 44), the incident separation lines do not coalesce near the center of the region, but rather continue farther downstream almost in parallel until they converge at $x \approx 110$ mm to form a narrow band of skin friction lines (3), which are offset to the left side of the channel. The band represents the surface image of the boundary between the left and right vortices generated by the incident single fin interactions. Lines of divergence are also apparent near the right fin (4) and left fin (5) associated with the incident single fin inter-

action. The second line of coalescence observed in the $k-\epsilon$ Chien results (4 in Fig. 43) is not present in this computation. Consequently, the $k-\epsilon$ Knight model does not predict a secondary separation underneath the left side of the right vortex. The difference is due to deviation in the predictions of the pressure distribution in the spanwise direction, obtained with each turbulence model as described below.
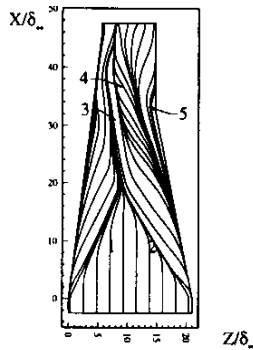

Figure 43: Computed skin friction lines $k-\epsilon$-Chien model (Case DF2)

1 Left incident separation line
2 Right incident separation line
3 Left downstream coalescence line
4 Right downstream coalescence line
5 Line of divergence (similar line near left fin)
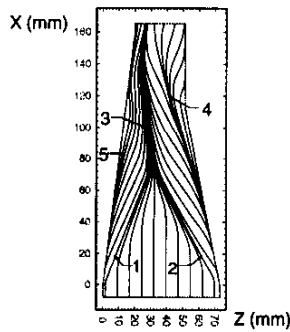
Figure 44: Computed skin friction lines $k-\epsilon$-Knight model (Case DF2)

1 Left incident separation line
2 Right incident separation line
3 Left downstream coalescence line
4,5 Lines of divergence

The surface pressure distribution in the spanwise direction at $x = 112$ mm is displayed in Figs. 46 and 47. The abscissa $z - z_{TML}$ represents the spanwise distance measured from the TML (Throat Middle Line). The computations

Figure 45: Experimental surface flow for $7° \times 11°$ (Case DF2)

using the $k-\epsilon$ Chien, $k-\epsilon$ Knight ("Present $k-\epsilon$"), and RSE models are in general agreement with the experiment, while the Spalart-Allmaras-Edwards, Baldwin-Lomax, and $k-\omega$ models overpredict the pressure by 16% to 21%. The $k-\epsilon$ Chien model predicts a local adverse pressure gradient in spanwise direction in the region -10 mm $< z - z_{TML} < -4$ mm. Since the flow near the surface at this location is moving towards the left fin, this adverse pressure gradient causes the secondary separation and the appearance of the right downstream coalescence line (4 in Fig. 43). The $k-\epsilon$ Knight model does not predict a significant adverse pressure gradient in this region, and hence a secondary separation line does not appear.
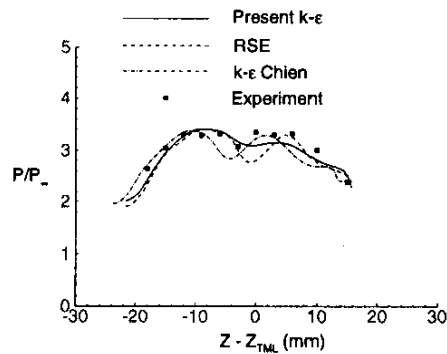

Figure 46: Wall pressure at $x = 112$ mm (Case DF2)

The surface pressure along the Throat Middle Line is displayed in Figs. 48 and 49. The computed and experimental surface pressure on TML are in good agreement for $x < 135$ mm for all models, although the computations slightly underestimate the extent of the upstream influ-
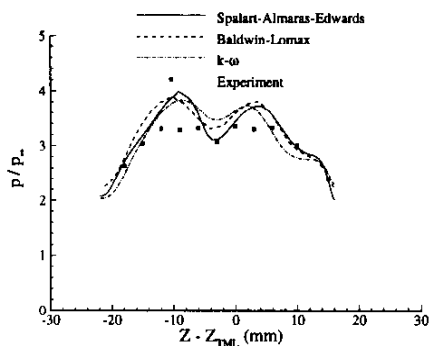
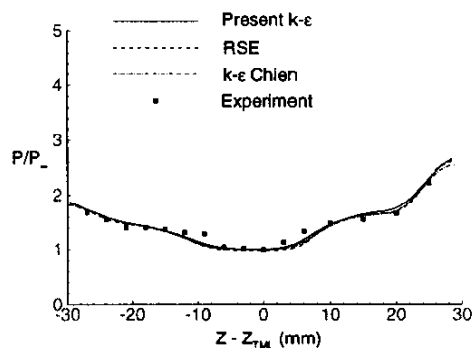Figure 47: Wall pressure at $x = 112$ mm (Case DF2)

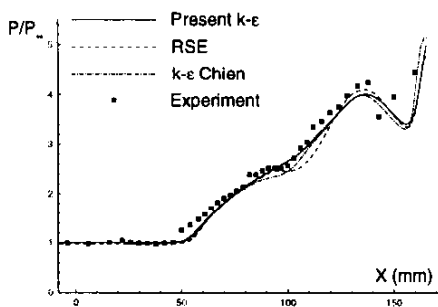Figure 50: Wall pressure at $x = 46$ mm (Case DF2)

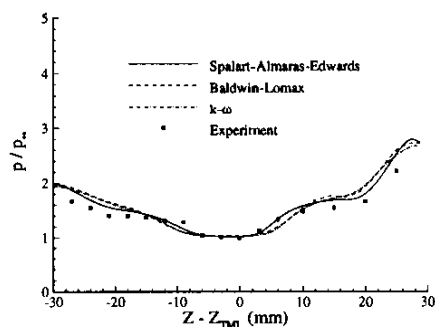

Figure 48: Wall pressure on TML (Case DF2)

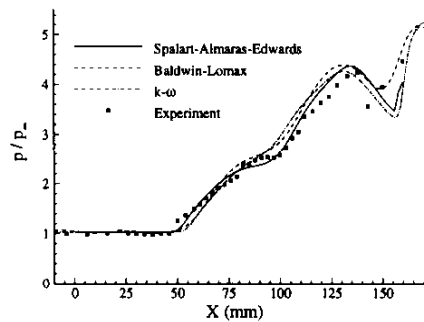Figure 51: Wall pressure at $x = 46$ mm (Case DF2)

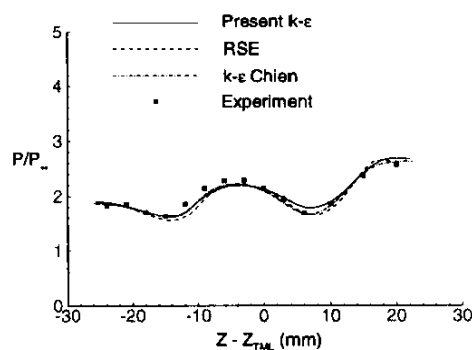Figure 49: Wall pressure on TML (Case DF2)
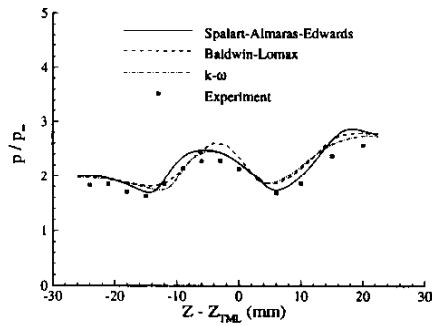

Figure 52: Wall pressure at $x = 79$ mm (Case DF2)

Figure 53: Wall pressure at $x = 79$ mm (Case DF2)

ence. The computed results in Fig. 48 do not accurately predict the pressure rise (beginning at $x = 145$ mm) associated with the shock reflection from the 7° fin, since the computations omit the boundary layers on the fin surfaces. The computed and experimental surface pressure at $x = 46$ and 79 mm are displayed in Figs. 50 to 53. Close agreement is again observed between the predictions of all models and experiment.

The surface heat transfer coefficient C_h is shown in Figs. 54 to 61. The heat transfer coefficient is defined by

$$C_h = \frac{Q_w(x,z)}{\rho_\infty U_\infty c_p (T_w(x,z) - T_{aw}(x,z))} \quad (2)$$

On the Throat Middle Line (Figs. 54 and 55), all turbulence models overpredict the heat transfer by approximately a factor of two downstream of the intersection of the shocks (which occurs at $x = 93.7$ mm). At $x = 46$ mm (Fig. 56 and 57), there is close agreement between the experiment and the $k - \epsilon$ Knight, $k - \epsilon$ Chien, and RSE models, while the Spalart-Allmaras-Edwards, Baldwin-Lomax and k–ω models show some discrepancies with the experiment. Note, however, that nearly all the experimental data at this location are situated in the nominally 2-D incoming boundary layer. A similar conclusion holds at $x = 79$ mm (Fig. 58 and 59), where again most of the experimental data are within the nominally 2-D boundary layer. At $x = 112$ mm (Figs. 60 and 61), located within the strongly 3-D region of the flow, all models show significant disagreement with the experiment.

The overprediction in C_h represents an overestimate in Q_w, since a series of studies [44, 45] have

demonstrated that the computed Q_w is proportional to the computed $T_w - T_{aw}$. A possible explanation [46] is that the turbulence models overestimate the effects of the shock-boundary layer interaction on the turbulence production, thereby generating excessive turbulence kinetic energy and turbulent eddy viscosity, and thus overestimating the turbulent thermal conductivity.
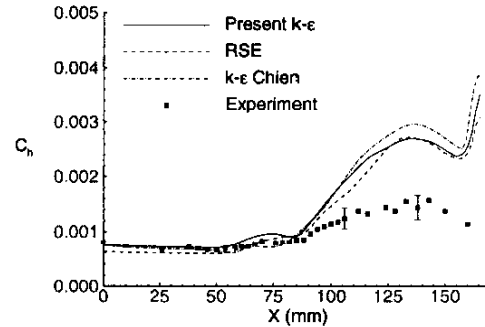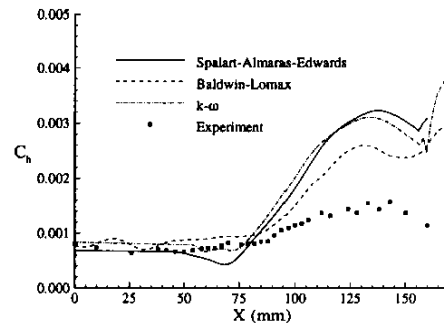

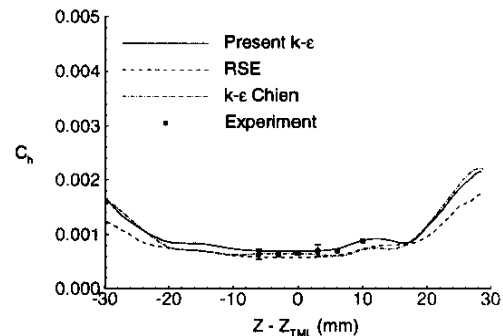Figure 54: C_h on TML (Case DF2)

Figure 55: C_h on TML (Case DF2)

Figure 56: C_h at $x = 46$ mm (Case DF2)

The adiabatic wall temperature T_{aw}/T_∞ is shown in Figs. 62 to 69, respectively. The $k - \epsilon$
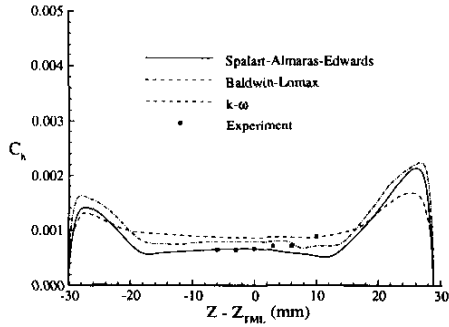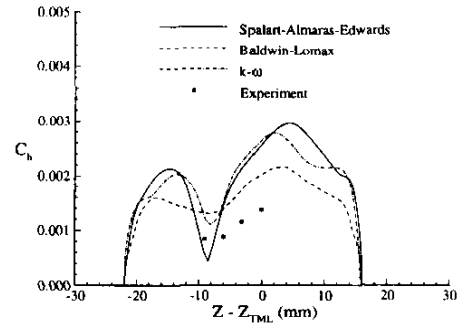
Figure 57: C_h at $x = 46$ mm (Case DF2)

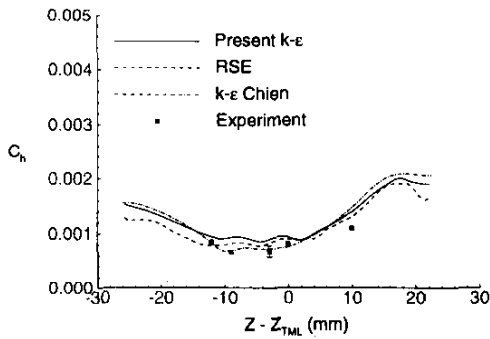Figure 58: C_h at $x = 79$ mm (Case DF2)

Figure 59: C_h at $x = 79$ mm (Case DF2)

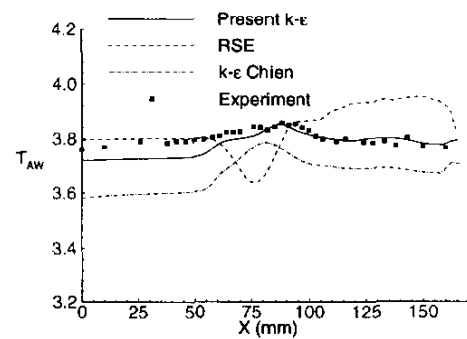Figure 60: C_h at $x = 112$ mm (Case DF2)

Figure 61: C_h at $x = 112$ mm (Case DF2)
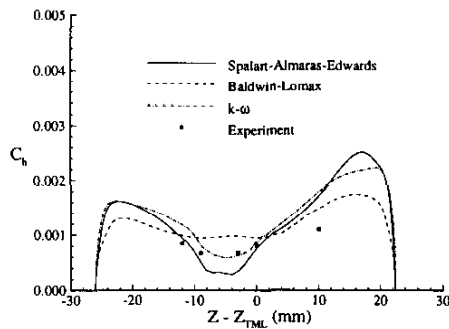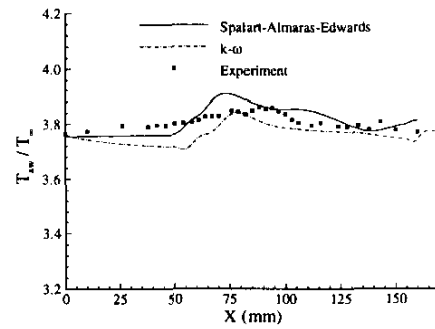
Figure 62: T_{aw} on TML (Case DF2)
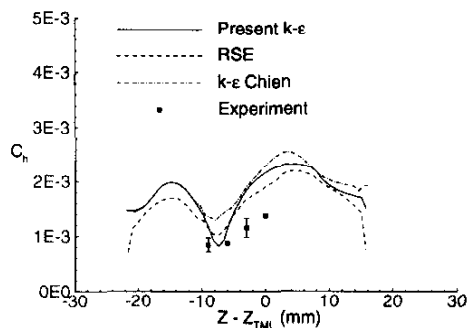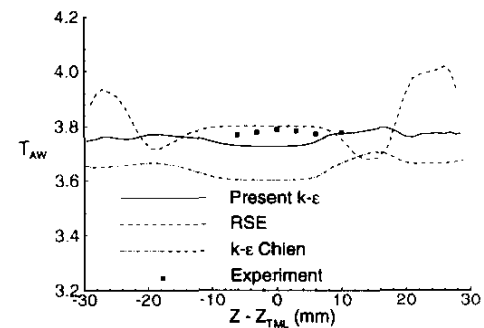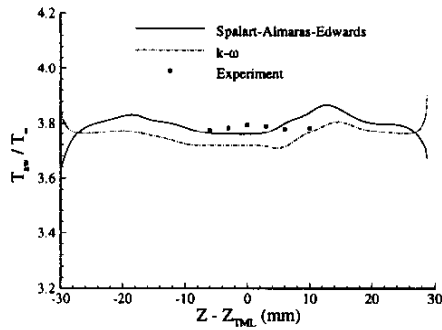
Figure 63: T_{aw} on TML (Case DF2)
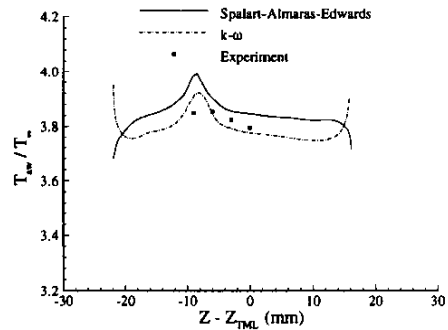
Figure 64: T_{aw} at $x = 46$ mm (Case DF2)
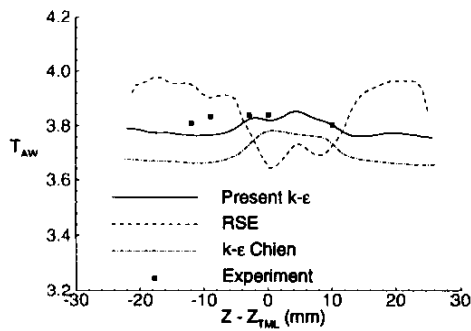
Figure 65: T_{aw} at $x = 46$ mm (Case DF2)

Figure 66: T_{aw} at $x = 79$ mm (Case DF2)

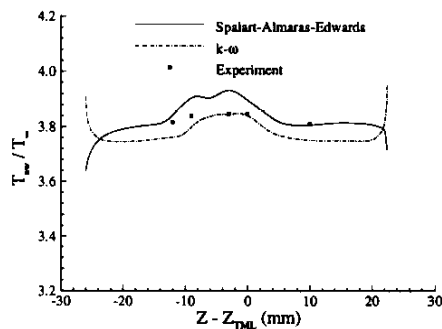Figure 67: T_{aw} at $x = 79$ mm (Case DF2)
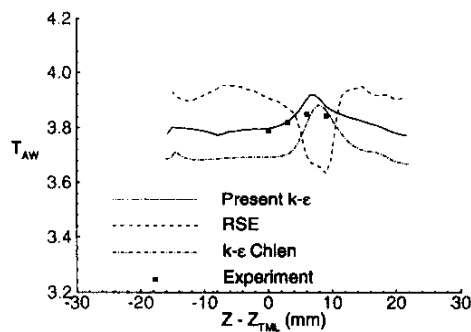
Figure 68: T_{aw} at $x = 112$ mm (Case DF2)

Figure 69: T_{aw} at $x = 112$ mm (Case DF2)

Knight and $k - \omega$ models display closest agreement with experiment.

3.3 Case DF3

The surface pressure on the centerline is shown in Fig. 70. The Baldwin-Lomax (IB) model displays virtually identical results for the second-order accurate [R2] and third-order accurate [R3] implementations of the inviscid flux using Roe's method [47]. The location of the beginning of the pressure rise (the "upstream influence") is underestimated, and the pressure downstream of the plateau region is overestimated. The Baldwin-Lomax-Panaras model provides the best prediction of surface pressure, although underestimating the peak pressure by 16%. The Spalart-Allmaras-Edwards model accurately predicts the upstream influence, but overestimates the pressure downstream of the plateau region, and underestimates the peak pressure. The $k - \epsilon$ model accurately predicts the upstream influence, but overestimates the surface pressure elsewhere.

Figure 70: Surface pressure (Case DF3)

The skin friction coefficient c_f on the centerline is displayed in Fig. 71. Several turbulence models accurately predict the onset of separation, namely, Baldwin-Lomax-Pana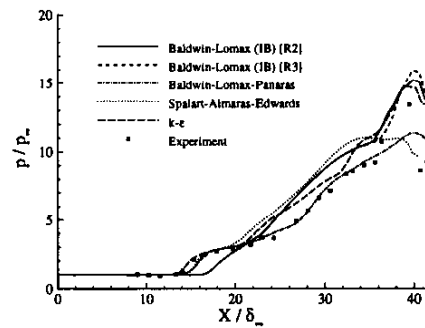ras, $k-\epsilon$ (with compressibility correction), $k-\epsilon$ (Rodi-Horstman) and $k-\epsilon$ (Vuong-Coakley). However, all turbulence models fail to accurately predict the skin friction downstream. The wide range of the predictions is reminiscent of the scatter in 2-D turbulent compression corner simulations [48].
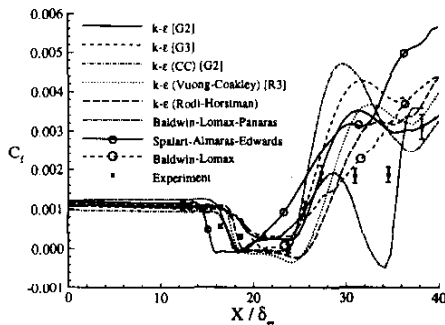
Figure 71: Skin friction on centerline (Case DF3)

The skin friction results at $x = 25.3\delta_\infty$ are shown in Fig. 72. The computations again display generally poor agreement with experiment. The Baldwin-Lomax-Panaras model displays the smallest error.
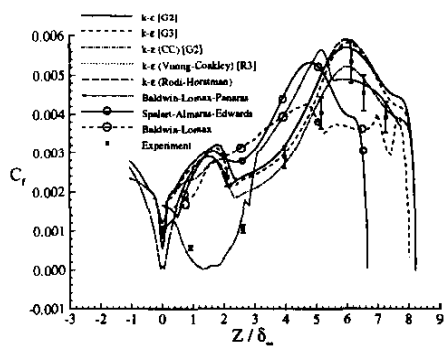
Figure 72: Skin friction at $x = 25.3\delta_\infty$ (Case DF3)

The experimental pitot pressure p_p/p_{p_∞} contours at $x = 32.33\delta_\infty$ are presented in Fig. 73. One half of the cross section is shown, as experimental surveys demonstrated the symmetry of the flowfield [49]. The principal features include the low pitot pressure region near the centerline
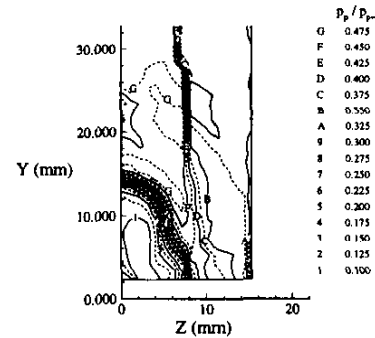
Figure 73: Experimental p_p at $x = 32.3\delta_\infty$ (Case DF3)
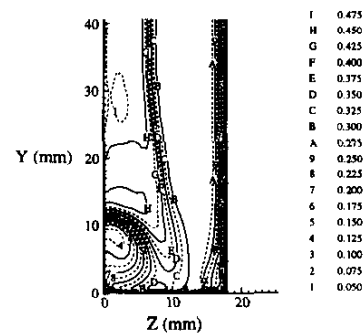
Figure 74: Computed p_p at $x = 32.3\delta_\infty$ using Baldwin-Lomax [IB] (Case DF3)
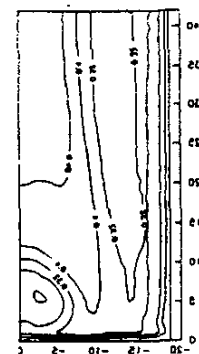
Figure 75: Computed p_p at $x = 32.3\delta_\infty$ using Baldwin-Lomax model (Case DF3)
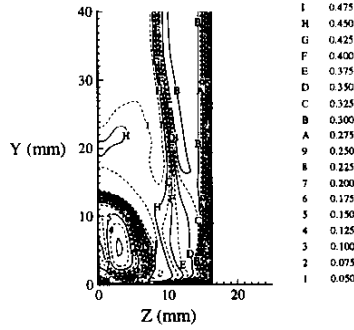
Figure 76: Computed p_p at $x = 32.3\delta_\infty$ using Spalart-Allmaras-Edwards model (Case DF3)

and the inviscid shock.

The computed pitot pressure using the Baldwin-Lomax model is shown in Figs. 74 and 75. The computed width of the low p_p region is in reasonable agreement with the experiment, although the height is somewhat greater. Closer agreement is observed with the Spalart-Allmaras-Edwards model (Fig. 76).

3.4 Case DF4

The surface pressure on the centerline is presented in Figs. 77 and 78. The agreement is good. All turbulence models accurately predict the location of the beginning of the pressure rise (the upstream influence). The Baldwin-Lomax model using the Buleev Integral length scale overestimates the peak pressure by 30%. The expansion fan ($7 \leq x/\delta_\infty \leq 8.5$) and subsequent second interaction ($8.5 \leq x/\delta_\infty \leq 10$) are accurately predicted by all models except the $k - \epsilon$ Rodi model[6].

Figs. 79 and 82 display surface pressure at $x = 5.6\ \delta_\infty$. The pressure is overestimated typically by 30% at the centerline (see Figs. 77 and 78) and underestimated by at most a comparable amount off centerline. The results of all turbulence models are similar, with the exception of Baldwin-Lomax (Fig. 79). Figs. 80 and 82 display surface pressure at $x = 6.9\delta_\infty$. The re-

---

[6]In the experiment, the boundary layers on the fins separate at $x \approx 6.5\delta_\infty$ due to the impingement of the shock waves. The $k-\epsilon$ Rodi model does not predict separation on the fins. Consequently, the computed reflected shocks are stronger, thereby leading to higher pressure at $x \approx 10\delta_\infty$.
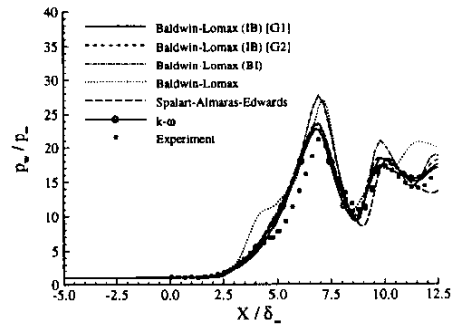

Figure 77: Surface pressure on centerline (Case DF4)
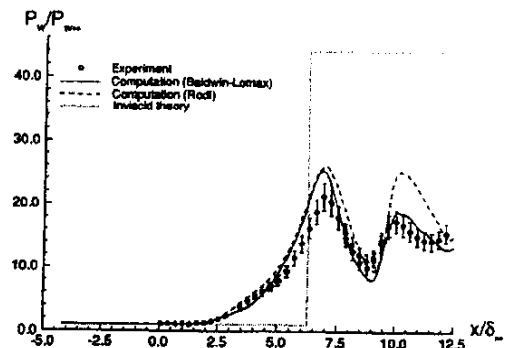
Figure 78: Surface pressure on centerline (Case DF4)
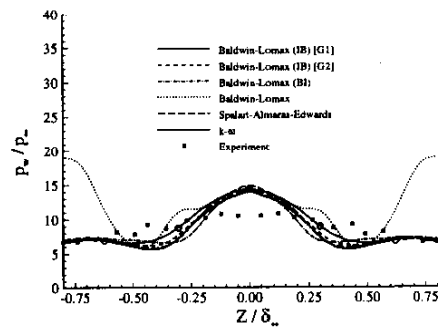
Figure 79: Surface pressure at $x = 5.6\delta_\infty$ (Case DF4)
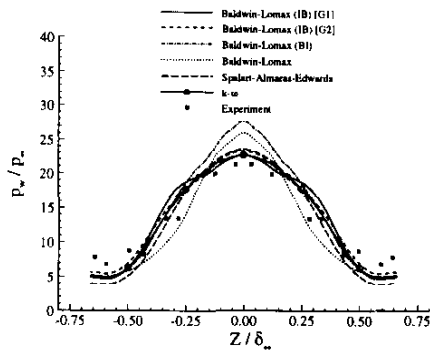
Figure 80: Surface pressure at $x = 6.9\delta_\infty$ (Case DF4)
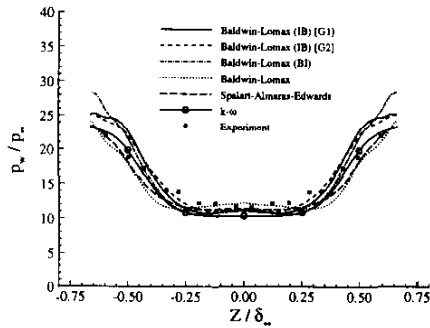
Figure 81: Surface pressure at $x = 8.3\delta_\infty$ (Case DF4)
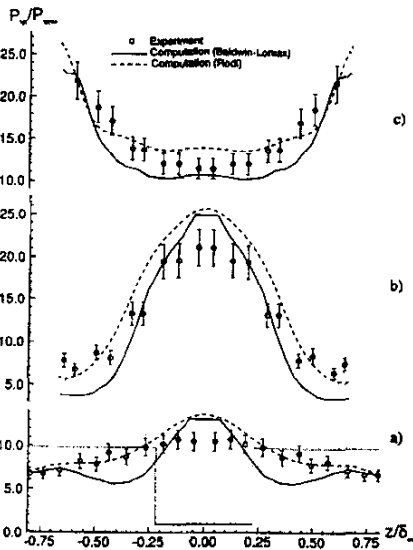
Figure 82: Surface pressure at $x = 5.6, 6.9$ and $8.3\delta_\infty$ (Case DF4)

sults of most turbulence models are similar, and in good agreement with the experiment. The Baldwin-Lomax model (Buleev Integral) overestimates the centerline pressure by 30%. Figs. 81 and 82 display surface pressure at $x = 8.3\delta_\infty$. All turbulence models are in good agreement with the experiment.

The surface heat transfer Q_w on the centerline is displayed in Figs. 83 and 84. With the exception of the Baldwin-Lomax model with the Buleev Integral length scale, there is generally good agreement with the experiment. However, away from the centerline, the agreement becomes increasingly poor with distance downstream, as shown at $x = 5.08\delta_\infty$ (Figs. 85 and 86), at $x = 6.4\delta_\infty$ (Figs. 87 and 88), and at $x = 7.78\delta_\infty$ (Figs. 89 and 90) where the maximum deviation from experiment ranges from 40% to 150%.
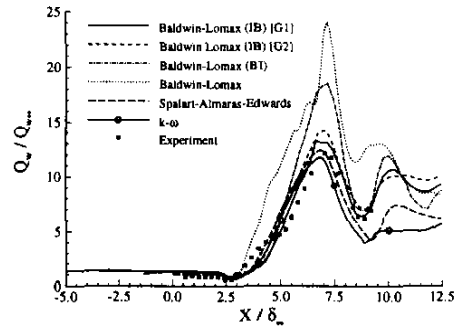
Figure 83: Surface heat transfer on centerline (Case DF4)
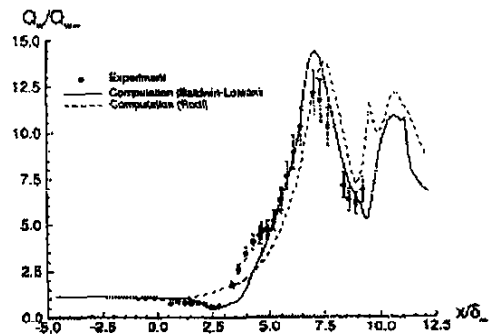
Figure 84: Surface heat transfer on centerline (Case DF4)

The surface streamline angle Φ, measured relative to the freestream direction x, is presented at $x = 5.6\delta_\infty$ (Fig. 91), $6.9\delta_\infty$ (Fig. 92) and
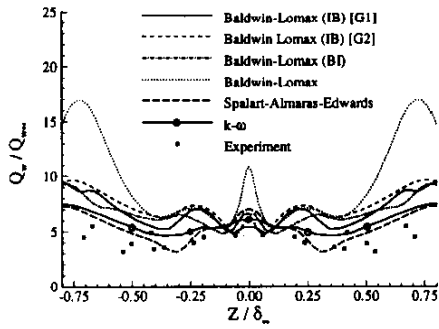
Figure 85: Surface heat transfer at x = $5.08\delta_\infty$ (Case DF4)

Figure 88: Surface heat transfer at x = $6.4\delta_\infty$ (Case DF4). See Fig. 84 for legend.

Figure 86: Surface heat transfer at x = $5.08\delta_\infty$ (Case DF4). See Fig. 84 for legend.
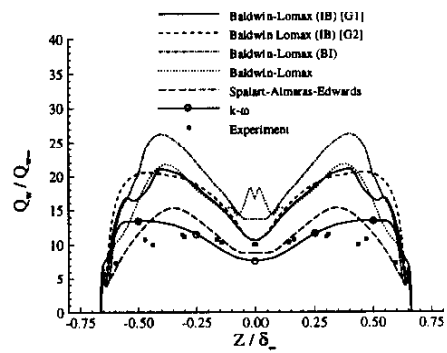
Figure 89: Surface heat transfer at x = $7.78\delta_\infty$ (Case DF4)

Figure 87: Surface heat transfer at x = $6.4\delta_\infty$ (Case DF4)
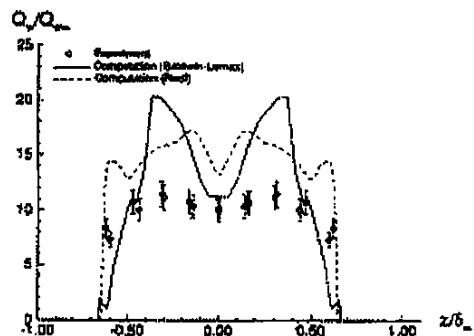
Figure 90: Surface heat transfer at x = $7.78\delta_\infty$ (Case DF4). See Fig. 84 for legend.

$8.3\delta_\infty$ (Fig. 93) for the Baldwin-Lomax model by using Inverse Blending and Buleev Integral length scales. The agreement is poor.
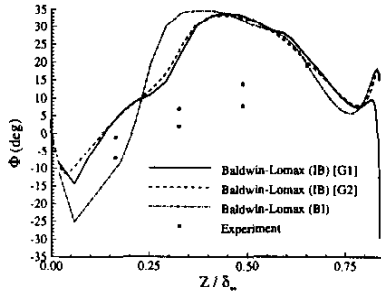
Figure 91: Surface streamline angle at $x = 5.6\delta_\infty$ (Case DF4)
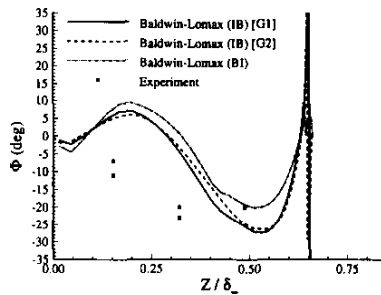
Figure 92: Surface streamline angle at $x = 6.9\delta_\infty$ (Case DF4)
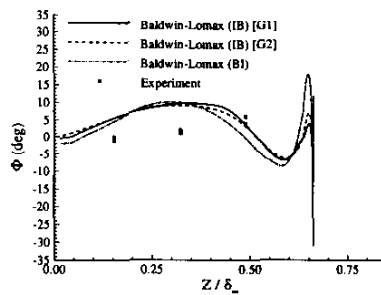
Figure 93: Surface streamline angle at $x = 8.3\delta_\infty$ (Case DF4)

Yaw angle profiles at $x = 5.6\delta_\infty$ and $z/\delta_\infty = 0.16, 0.33, 0.49$, and 0.65 are shown in Figs. 94 to 97, and pitot pressure profiles at the same locations (plus $z = 0$) in Figs. 98 to 102, respectively. The principal features of both the yaw angle and pitot pressure profiles are generally predicted by all turbulence models.
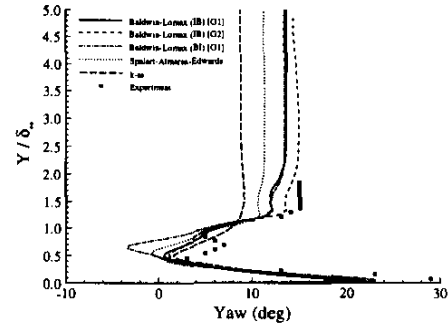
Figure 94: Yaw angle at $x = 5.6\delta_\infty$ and $z = 0.16\delta_\infty$ (Case DF4)
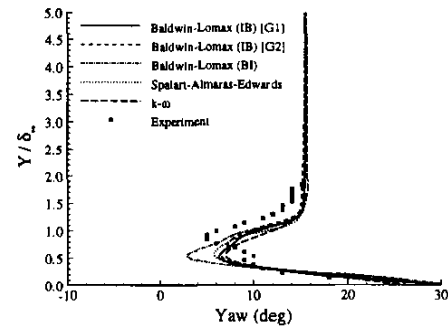
Figure 95: Yaw angle at $x = 5.6\delta_\infty$ and $z = 0.33\delta_\infty$ (Case DF4)
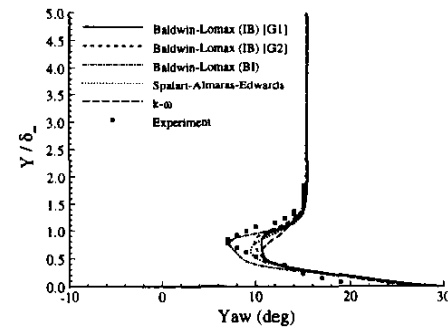
Figure 96: Yaw angle at $x = 5.6\delta_\infty$ and $z = 0.49\delta_\infty$ (Case DF4)
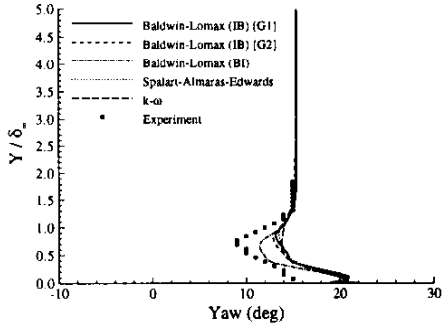
Figure 97: Yaw angle at $x = 5.6\delta_\infty$ and $z = 0.65\delta_\infty$ (Case DF4)
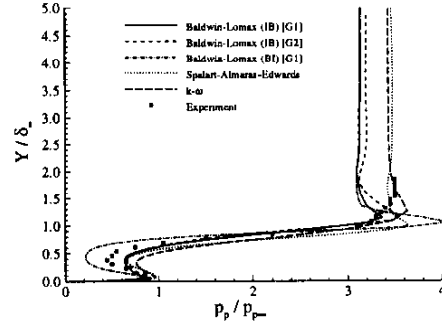
Figure 100: p_p at $x = 5.6\delta_\infty$ and $z = 0.33\delta_\infty$ (Case DF4)
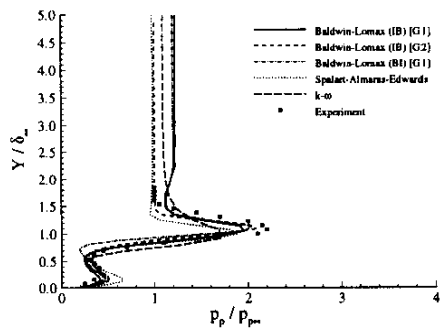
Figure 98: p_p at $x = 5.6\delta_\infty$ and $z = 0$ (Case DF4)
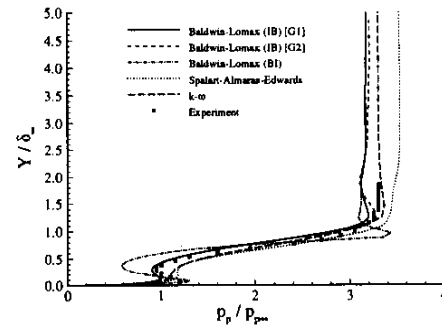
Figure 101: p_p at $x = 5.6\delta_\infty$ and $z = 0.49\delta_\infty$ (Case DF4)
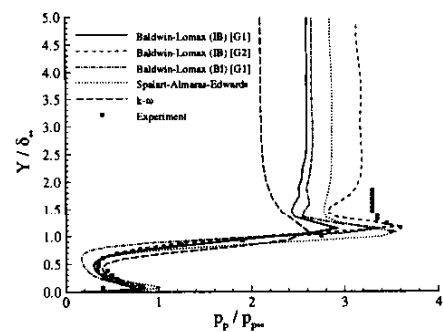
Figure 99: p_p at $x = 5.6\delta_\infty$ and $z = 0.16\delta_\infty$ (Case DF4)
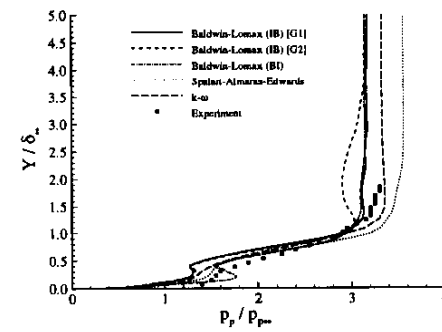
Figure 102: p_p at $x = 5.6\delta_\infty$ and $z = 0.65\delta_\infty$ (Case DF4)

4 Hollow-cylinder flare

The hollow-cylinder flare geometry is shown in Fig. 103. It is the axisymmetric counterpart
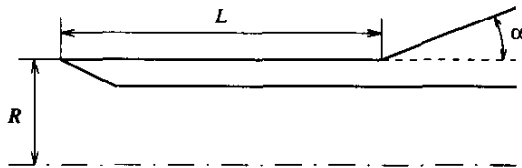
Figure 103: Hollow-cylinder flare model geometry

of the well-known compression ramp geometry. The flare generates a conical shock wave which interacts with the boundary layer developing on the cylinder. The flow parameters are the Mach number M_∞, the Reynolds number Re_∞ based on the leading-edge-to-flare-hinge distance L, the flare angle α and the wall temperature ration T_w/T_∞[7]. The Reynolds number determines, in particular, the state of the boundary layer upstream of the interaction and therefore the nature of the interaction.

The flowfield structure of the hollow cylinder flare interaction is similar to that of the compression ramp flow which has been described in detail in several review reports [50, 4], in particular in the article by Délery and Panaras in the first report of this Working Group [9]. It is schematically represented on Fig. 104 for the

Figure 104: Hypersonic ramp flow. Sketch of the flowfield

case of a separated turbulent hypersonic interaction. At the beginning of the interaction, the

boundary layer starts thickening and eventually separates at point S. The thickening is responsible for the generation of compression waves which rapidly coalesce into a separation shock. The separated shear layer eventually reattaches on the wedge (flare for the axisymmetric configuration) where it produces a strong reattachment shock. The reattachment shock intersects the separation shock at the triple point I leading to the formation of the transmitted global compression shock and of a reflected expansion fan. Since for hypersonic flows the separation shock makes a small angle with the flat plate (or cylinder), the triple point I is quite close to the wall so that the reflected expansion reaches the wall only slightly downstream of reattachment. Laminar interactions are characterized by much more extended separation zones as well as by a smoother compression upstream of separation. The axisymmetric interaction differs from the 2-D interaction by weaker shock angles for a given deviation and by the non-uniformity of the flow downstream of a conical shock, although this latter effect is hardly noticeable for the cases under consideration.

Two configurations (a laminar configuration refered to as HCFL and a turbulent one refered to as HCFT) were computed by one or more participants. The flow conditions are shown in Table 9. The laminar case was

Table 9: Hollow-cylinder flare cases

Case	Ref	M_∞	α	Re_∞ ($\times 10^3$)	$T_w/T_{t\infty}$
HCFL	[51]	9.90	30°	18.9	0.276
HCFT	[52]	5.01	35°	11025	0.60

computed by six participants, four computations using a cell-centered finite volume Navier-Stokes (FVNS) solver, one using an unstructured grid residual distribution Navier-Stokes (RDNS) solver [53] and one a direct simulation Monte Carlo (DSMC) solver [54]. A detailed comparison of a subset of these computations with the experimental data by Chanetz [51] is presented in [55]. The turbulent case was computed by one participant using a Reynolds averaged Navier-Stokes solver with the Spalart-Allmaras turbulence model [56]. The simulations are summarized in Table 10.

[7]For completeness, one should add the Reynolds number based on the cylinder outer radius, which controls the axisymmetry effects on the incoming boundary layer itself (transverse curvature effect). This effect is negligible for large Reynolds numbers, for which the boundary layer develops exactly as on a flat plate.

Table 10: Participants for the hollow cylinder-flare cases

Participant (code)/case	HCFL	HCFT
J.-M. Bousquet (FLU3M)	FVNS	
R. Bur (NASCA)	FVNS	
G. Degrez et al. (VKI-MB)	FVNS	FVRANS
F. Grasso (HIG-2XP)	FVNS	
J. Moss (DSMC)	DSMC	
E. Van der Weide (IcARus)	RDNS	

4.1 Case HCFL

Grid refinement studies have been performed both by Bousquet, who used a sequence of grids containing 101×39, 201×77 and 401×153 points in the longitudinal and normal directions respectively, and by Tombarel and Degrez, who used a sequence of grids containing 101×26, 201×51 and 401×101 points. The sensitivity of the results to the grid density is illustrated in Fig. 105, which shows Stanton number dis-
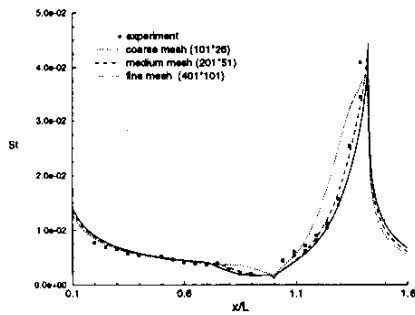
Figure 105: Stanton number distribution, grid sensitivity study (HCFL)

tributions as computed by Tombarel and De-grez. One sees that grid independence is not proven even for the finest mesh, since the finest mesh results are still noticeably different from the medium mesh results. As far as the calculations by Bousquet are concerned, only the fine grid results have been provided, but the author reports an excellent spatial convergence. Note that the latter grids are finer in the normal direction than those used by Tombarel and Degrez, which could explain a better grid convergence.

Surface pressure coefficient distributions computed by all six participants are shown on Fig. 106. First, one notices that all codes agree on the cylinder upstream of the interaction, but
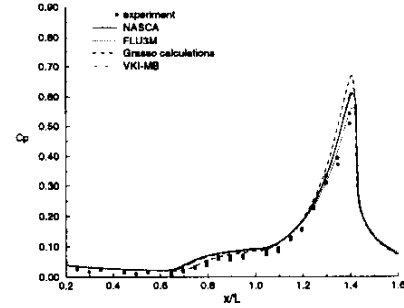
(a) Finite volume Navier-Stokes computations
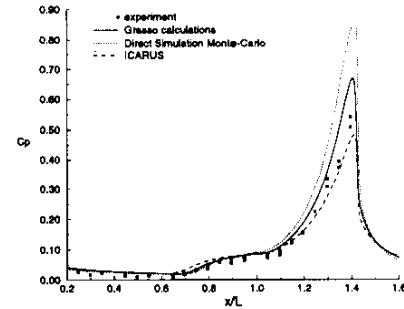
(b) IcARus, DSMC and HIG-2XP computations

Figure 106: Surface pressure coefficient distributions (HCFL)

the computed pressure coefficients are higher than the measured values, possibly due to some offset in the experimental values. One notices that the FLU3M, NASCA and VKI-MB results are nearly identical. The starting location of the pressure rise is seen to be slightly upstream of the experimental one (slightly overevaluated upstream influence) for these computations and for the IcARus unstructured grid computation while it is about at the experimental position for the HIP-2XP (Grasso) computation and slightly downstream for the DSMC computation.

At this stage, it should be noticed that slightly different freestream conditions were imposed by the various participants. Whereas the incoming freestream Mach number was set at 9.90 for the NASCA, VKI-MB, IcARus and DSMC computations as specified in [9], a value of 9.95 was used for the FLU3M computation which was performed before the experiment and a value of 9.91, closest to the real experimental one, for the HIP-2XP (Grasso) computation. Other slight differences concern the stagnation temperature (1070°K for the NASCA computation, 1050°K

for all others) and the wall temperature (295°K for the DSMC computation, and 290°K for all others). These small variations in freestream conditions however are not deemed to have a significant impact on the computational results.

More substantial differences between computed pressure distributions are observed on the flare. In particular, the DSMC computation strongly overevaluates the pressure on the flare while the IcARus computation underevaluates it, possibly indicating an insufficient grid resolution on the flare for this computation. Finite volume Navier-Stokes computations are in closer agreement between themselves and with the experiment, the HIP-2XP computation giving the highest values, followed by the NASCA and VKI-MB computations, which give essentially identical results, and finally by the FLU3M computation, which gives the lowest values[8]. The latter computation appears to be in closest agreement with the experiment, but one should keep in mind the possible pressure offset in the experiments mentioned earlier.

Computed skin friction distributions are shown on Fig. 107. Important differences are observed in the separation and reattachment regions. Just as for the pressure distributions, the FLU3M, NASCA, and VKI-MB computations give essentially identical results with a separation point at a reduced abscissa $x/L = 0.72$ and a reattachment point at $x/L = 1.34$, to be compared with the experimental values obtained by an oil flow visualization $x_{sep}/L = 0.77$ and $x_{rea}/L = 1.31$. The IcARuS unstructured grid computation also gives very similar results. The HIP-2XP (Grasso) results are seen to be in better agreement with the experimental values while the DSMC computation underpredicts the size of the separation bubble. Experimental and computed separation and reattachment point locations are summarized in Table 11.

Finally, experimental and computed Stanton number distributions are shown on Fig. 108. The trends observed for the pressure coefficient and skin friction distributions are confirmed, i.e., the underprediction of the size of the separation bubble by the DSMC computation, the better match with the experimental results given by the HIP-2XP (Grasso) computation, and

[8]The slightly higher freestream Mach number value used in this computation may play a role here.
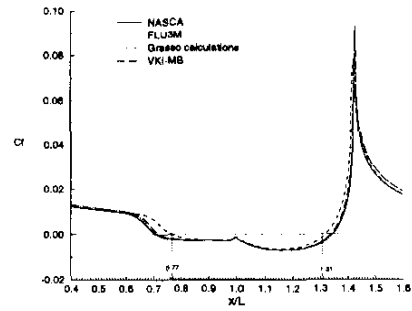
(a) Finite volume Navier-Stokes computations
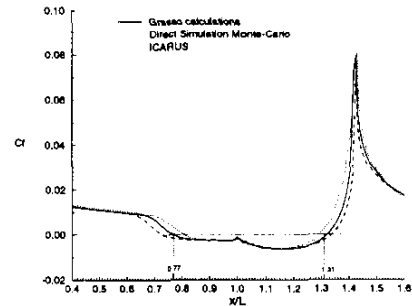
(b) IcARus, DSMC and HIG-2XP computations

Figure 107: Skin friction coefficient distributions (HCFL)

Table 11: Separation-reattachment point locations (HCFL)

code/abscissa	sep.	reatt.
J.-M. Bousquet (FLU3M)	0.72	1.34
R. Bur (NASCA)	0.72	1.34
G. Degrez et al. (VKI-MB)	0.73	1.34
F. Grasso (HIG-2XP)	0.77	1.32
J. Moss (DSMC)	0.81	1.29
E. Van der Weide (IcARus)	0.73	1.34
experiment [51]	0.77	1.31

the close agreement between the remaining four computations (FLU3M, NASCA, VKI-MB and IcARus) which predict a slightly oversized separation bubble.

4.2 Case HCFT

This test case was computed by Paciorri et al. [57] on different grids. The initial coarse grid contained 100 × 50 points and used a uniform stretching in the normal direction. A second adapted 100 × 50 grid was then produced
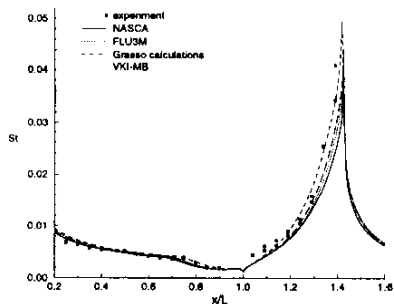
(a) Finite volume Navier-Stokes computations
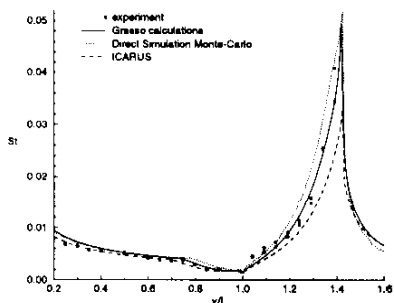
(b) IcARus, DSMC, and HIG-2XP computations

Figure 108: Stanton number distributions (HCFL)

in which the normal stretching was made variable along the wall to cluster grid lines closer to the wall in the vicinity and downstream of reattachment where the boundary layer is very thin. This clustering is illustrated in Fig. 109 which compares both grids. The corresponding first grid line y^+ distributions are shown in Fig. 110, where one observes that, thanks to the increased clustering normal to the wall in the reattachment region, the wall coordinate y^+ never exceeds 2 for the adapted grid, whereas it reaches a value of 6 in the reattachment region for the initial grid. Finally, a fine 200×100 grid was obtained by refining the adapted grid by a factor of two in each direction.

Surface pressure distributions are shown on Fig. 111. Although there is a good agreement between computed results, the extent of the separated zone is seen to be strongly underestimated. In particular, the computed pressure rise at separation is well downstream of the experimental position. One also notices a slight disagreement between computed and experimental values downstream of reattachment.
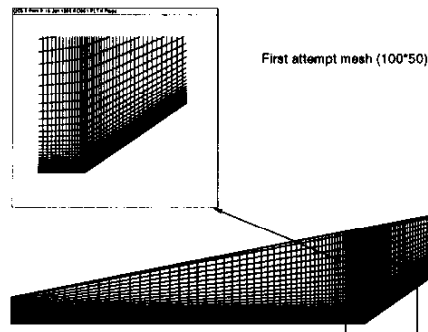
(a) Initial grid
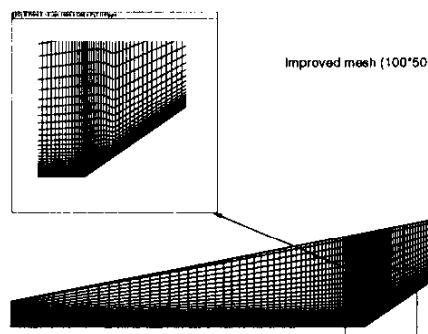
(b) Adapted grid

Figure 109: Coarse grids for HCFT test case
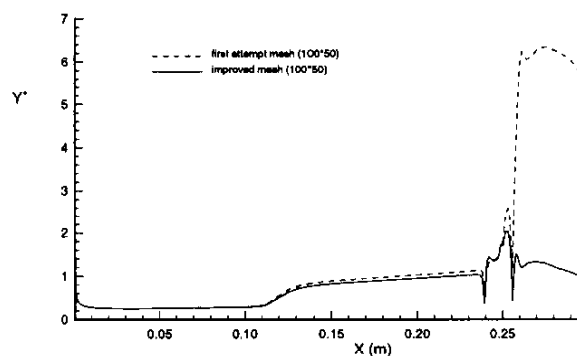
Figure 110: First grid line y^+ distributions on coarse meshes (HCFT)
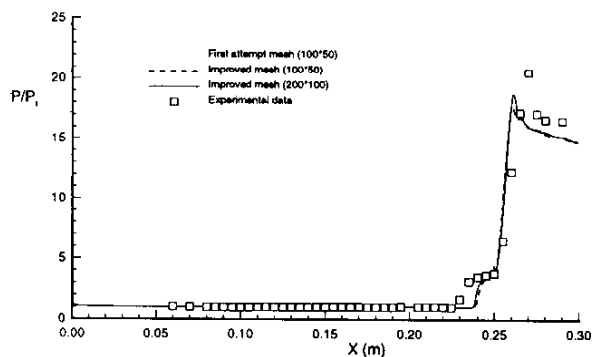
Figure 111: Surface pressure coefficient distributions (HCFT)

Stanton number distributions are shown on Fig. 112. Here, the effect of grid adaption is clearly visible. While the initial grid fails completely to predict the Stanton number at reattachment and downstream, the adapted grid results are in reasonable agreement with the experimental data both in terms of the peak value and of the distribution downstream of reattachment. The computed peak heat transfer location, however, is upstream of the experimental position because of the underestimation of the separated bubble size. The discrepancy between the computed and experimental separation bubble size is also the reason for the disagreement between computed and experimental values near the separation point.
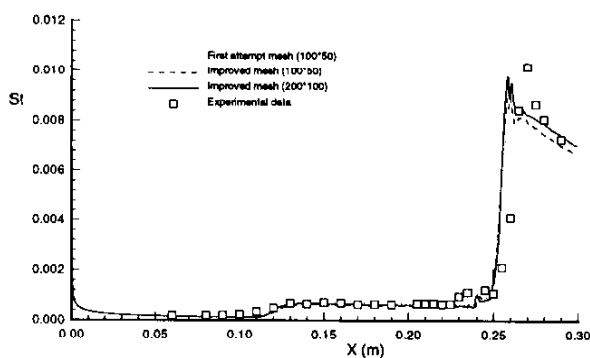
Figure 112: Stanton number distributions (HCFT)

5 Conclusions

The objective of the present study was to review the capabilities of current CFD solvers to predict quantities of interest for designers of high-speed vehicles, namely mean and fluctuating (RMS) aerodynamic (pressure, skin friction) and thermal (heat transfer) loads as well as flowfield structure (occurrence of separation and of vortical flow structures). Laminar and turbulent interactions are examined successively.

5.1 Laminar interactions

For laminar interactions, present CFD technology allows accurate prediction of both aerodynamic and thermal loads. For strong interactions at relatively high Reynolds numbers, though, extremely fine and carefully generated grids are necessary to obtain accurate results (at least 200×75 points for nominally 2-D interactions and therefore, by extrapolations, at least 1.5 million points for 3-D interactions) because of the extremely high aspect ratio of laminar separated flow regions. Adaptivity thus appears essential to accurately calculate 3-D interactions at an affordable cost.

5.2 Turbulent interactions

For 3-D interactions, mean pressure distributions are generally predicted satisfactorily, with little variation between computations using different turbulence models. The satisfactory pressure predictions may be attributable to an approximate triple-deck structure of the flowfield [25] (see, for example, Inger [58, 59, 60] who extended the original work of Stewartson [61] to nonseparated 3-D shock wave turbulent boundary layer interactions). In the first layer ("deck"), located immediately adjacent to the surface, the flow is controlled by both viscous (i.e., laminar and turbulent stresses and heat transfer) and inviscid effects. In the second layer, immediately above the first deck, the flow is rotational and inviscid to a first approximation; i.e., turbulent stresses and heat transfer are higher order effects. This region comprises most of the boundary layer in the interaction. The third region is the inviscid, irrotational flow outside the boundary layer. The surface

pressure distribution is, to a first approximation, determined by the interaction of the second and third layers and is therefore insensitive to the turbulence model. In effect, the turbulence model provides the proper vorticity distribution in the incoming boundary layer, but does not otherwise significantly affect the surface pressure. Since all turbulence models provide the appropriate flat plate boundary layer profile as inflow, there is little difference in the prediction of surface pressure.

For nominally 2-D interactions, however, satisfactory prediction of mean pressure distributions is achieved typically only for weak interactions. For strong interactions, computed pressure distributions are generally in poor agreement with the experiment[9] for two reasons. First, the flow exhibits a high level of unsteadiness, which is not captured by any of the RANS computations [65] (see below). Second, eddy viscosity models use a single length scale to characterize the turbulence characteristics which, while valid for attached boundary layer flow, ceases to be correct in the presence of separation bubbles. In addition, many eddy viscosity models use wall functions which lose their validity in the neighbourhood of 2-D separation and reattachment points.

As far as the 3-D flowfield structure is concerned, primary separation is generally well predicted whereas secondary separation appears to be very sensitive to the turbulence model and is not predicted accurately in most cases.

For 3-D interactions, boundary layer profiles of pitot pressure and yaw angle are reasonably predicted for weak interactions but accuracy degrades as interaction strength increases. The concept of a triple-deck structure (described above) would explain the general insensitivity of the computed profiles to the turbulence model, since the middle deck occupies most of the boundary layer.

Skin friction and heat transfer distribution predictions are generally poor, except for weak interactions, and significant differences are evident between turbulence models. Differences of up to

100% between experimental and numerical results were obtained for strong interactions.

None of the RANS computations captured the flowfield unsteadiness associated with shock wave motions observed in experimental studies, in particular for nominally 2-D interactions, and therefore no RANS computation was able to predict the fluctuating aerodynamic and thermal loads.

Ad hoc modifications of tubulence models such as proposed by Panaras improve the accuracy of numerical predictions, but the practical usefulness of such approaches is limited because the modifications required are strongly model dependent. Nevertheless, such studies are useful insofar as they are physically based (*e.g.*, the model of Panaras is based on the observation of a low turbulence region beneath the main vortex) and point out the deficiencies of standard models.

The previous conclusions lead to the following recommendations for further study.

- For turbulent interactions, it appears necessary to develop large eddy simulation solvers, as only LES models will allow us to predict the fluctuating pressure and heat transfer loads which can be very significant in shock wave/boundary layer interactions.

- Grid adaptivity strategies based on reliable error estimates are essential to allow accurate and affordable shock wave/boundary layer interaction computations.

- In order to continue making progress in turbulence modeling for shock wave / boundary layer interactions, it is essential to obtain accurate experimental data for

    - flowfield Reynolds stresses,
    - flowfield turbulent heat flux
    - wall pressure and heat transfer fluctuations.

---

[9] A notable exception are the predictions of Borisov *et al.* [62] and Bedarev *et al.* [63] for the 2-D compression corner using the $k - \omega$ model of Wilcox [64] which are in close agreement with the experiments of Zheltovodov.

6 Acknowledgments

References

[1] J. E. Greene. Interactions between Shock Waves and Turbulent Boundary Layers. In *Progress in Aerospace Science*, volume 11, pages 235–340. Pergammon Press, 1970.

[2] R. Korkegi. Survey of Viscous Interactions Associated with High Mach Number Flight. *AIAA Journal*, 9:771–784, May 1971.

[3] D. Peake and M. Tobak. Three-Dimensional Interactions and Vortical Flows with Emphasis on High Speed. Technical Report TM 81169, NASA, March 1980.

[4] J. Delery and J. Marvin. Shock-Wave Boundary-Layer Interactions. AGARDograph No. 280, February 1986.

[5] G. Settles and D. Dolling. Swept Shock Wave Boundary Layer Interactions. In *Tactical Missile Aerodynamics*, pages 297–379. AIAA, 1986.

[6] G. Settles and D. Dolling. Swept Shock / Boundary-Layer Interactions – Tutorial and Update. AIAA Paper 90-0375, 1990.

[7] J. Stollery. AGARD Special Course on Three-Dimensional Supersonic and Hypersonic Flows Including Separation. Advisory Group for Aerospace Research and Development, May 1989.

[8] G. Degrez, editor. *AGARD Special Course on Shock-Wave/Turbulent Boundary-Layer Interactions in Supersonic and Hypersonic Flow*. Advisory Group for Aerospace Research and Development, August 1993. AGARD Report 792.

[9] J. Delery and A. Panaras. Shock-Wave Boundary-Layer Interactions in High Mach Number Flows. AGARD AR-319, Volume 1, May 1996.

[10] A. Zheltovodov. Shock Waves / Turbulent Boundary Layer Interactions – Fundamental Studies and Applications. AIAA Paper No. 96-1977, 1996.

[11] F. Alvi and G. Settles. Physical Model of the Swept Shock / Boundary Layer Interaction Flowfield. *AIAA Journal*, 30:2252–2258, September 1992.

[12] A. Zheltovodov and E. Shilein. 3-D Swept Shock Waves / Turbulent Boundary Layer Interaction in Angles Configuration. Institute of Theoretical and Applied Mechanics, Russian Academy of Sciences, Siberian Division, Preprint No. 34-86, 1986.

[13] A. Zheltovodov. Physical Features and Some Properties of Two and Three-Dimensional Separated Flows at Supersonic Velocities. *Izvestiya AN SSSR, Mekhanika Zhidkosti i Gaza*, 3:42–50, 1979.

[14] A. Zheltovodov, A. Maksimov, and E. Shilein. Development of Turbulent Separated Flows in the Vicinity of Swept Shock Waves. In *The Interaction of Complex 3-D Flows*, pages 67–91. Institute of Theoretical and Applied Mechanics, USSR Academy of Sciences, Novosibirsk, Russia, 1987.

[15] M. Zubin and N. Ostapenko. Structure of the Flow in the Separation Region Resulting from Interaction of a Normal Shock Wave with a Boundary Layer in a Corner. *Izvestiya AN SSSR, Mekhanika Zhidkosti i Gaza*, 3:51–85, May-June 1979.

[16] P. Rodi, D. Dolling, and D. Knight. An Experimental/Computational Study of Heat

Transfer in Sharp Fin Induced Turbulent Interactions at Mach 5. AIAA Paper 91-1764, 1991.

[17] K. Kim, Y. Lee, F. Alvi, G. Settles, and C. Horstman. Laser Skin Friction Measurements and CFD Comparison of Weak-to-Strong Swept Shock / Boundary Layer Interactions, 1990. AIAA Paper No. 90-0378.

[18] D. Knight, C. Horstman, B. Shapey, and S. Bogdonoff. Structure of Supersonic Turbulent Flow Past a Sharp Fin. *AIAA Journal*, 25:1331–1337, 1987.

[19] M. Kussoy and K. Horstman. Documentation of Two- and Three Dimensional Shock-Wave/Turbulent Boundary Layer Interaction Flows at Mach 8.2. Technical Report NASA TM 103838, NASA Ames Research Center, May 1991.

[20] G. Settles and L. Dodson. Hypersonic Shock / Boundary Layer Interaction Database. Technical Report PSU-ME-90/91-003, Gas Dynamics Laboratory, Department of Mechanical Engineering, Penn State University, December 1990.

[21] J. Edwards and S. Chandra. Comparison of Eddy Viscosity-Transport Turbulencd Models for Three-Dimensional, Shock-Separated Flowfields. *AIAA Journal*, 34:756–763, 1996.

[22] W. Jones and B. Launder. The Prediction of Laminarization with a Two-Equation Model of Turbulence. *Int. Journal of Heat and Mass Transfer*, 15:301–304, 1972.

[23] B. Baldwin and H. Lomax. Thin Layer Approximation and Algebraic Model for Separated Flows. AIAA Paper 78-257, 1978.

[24] A. Panaras. Algebraic Turbulence Modelling for Swept Shock Wave / Turbulent Boundary Layer Interactions. Technical Report IB 223-96 A 22, Deutsche Forschungsanstalt für Luft- und Raumfahrt e.V., March 1996.

[25] D. Knight. Numerical Simulation of 3-D Shock Wave Turbulent Boundary Layer Interactions. In *AGARD/VKI Special Course on Shock-Wave Boundary-Layer Interactions in Supersonic and Hypersonic Flows*, pages 3-1 to 3-32. Von Karman Institute for Fluid Dynamics, May 1993. AGARD R-792.

[26] D. Gaitonde, J. Shang, and M. Visbal. Structure of a Double-Fin Interaction at High Speed. *AIAA Journal*, 33(2):193–200, February 1995.

[27] D. Gaitonde and J. Shang. Structure of a Turbulent Double-Fin Interaction at Mach 4. *AIAA Journal*, 33(12):2250–2258, December 1995.

[28] D. Gaitonde and J. Shang. On 3-D Shock Wave Turbulent Boundary Layer Interactions at Mach 4. AIAA Paper 96-0043, 1996.

[29] T. Garrison and G. Settles. Flowfield Visualization of Crossing Shock-Wave / Boundary Layer Interactions. AIAA Paper 92-0750, January 1992.

[30] T. Garrison, G. Settles, N. Narayanswami, and D. Knight. Structure of Crossing-Shock Wave/Turbulent Boundary Layer Interactions. *AIAA Journal*, 31:2204–2211, December 1993.

[31] T. Garrison and G. Settles. Interaction Strength and Model Geometry Effects on the Structure of Crossing - Shock Wave / Turbulent Boundary - Layer Interactions. AIAA Paper 93-0780, January 1993.

[32] D. Knight, T. Garrison, G. Settles, A. Zheltovodov, A. Maksimov, A. Shevchenko, and S. Vorontsov. Asymmetric Crossing-Shock Wave / Turbulent Boundary Layer Interaction. *AIAA Journal*, 33(12):2241–2249, Dec 1995.

[33] N. Narayanswami, D. Knight, S. Bogdonoff, and C. Horstman. Interaction Between Crossing Oblique Shocks and a Turbulent Boundary Layer. *AIAA Journal*, 30:1945–1952, August 1992.

[34] N. Narayanswami, D. Knight, and C. C. Horstman. Investigation of a Hypersonic Crossing Shock Wave / Turbulent Boundary Layer Interaction. *Shock Waves*, 3(1):35–48, 1993.

[35] N. Narayanswami, C. C. Horstman, and D. Knight. Computation of Crossing Shock Turbulent Boundary Layer Interaction at Mach 8.3. *AIAA Journal*, 31:1369–1376, August 1993.

[36] A. Zheltovodov, A. Maksimov, A. Shevchenko, S. Vorontsov, and D. Knight. Experimental Study and Computational Comparison of Crossing Shock Wave - Turbulent Boundary Layer Interaction. In *Proceedings of the International Conference on Methods of Aerophysical Research - Part 1*, pages 221–230, August 1994. Russian Academy of Sciences, Siberian Division.

[37] T. Garrison, G. Settles, N. Narayanswami, D. Knight, and C. Horstman. Flowfield Surveys and Computations of a Crossing Shock Wave / Boundary Layer Interaction. *AIAA Journal*, 34:50–56, Jan 1996.

[38] M. Kussoy and K. Horstman. Intersecting Shock-Wave/Turbulent Boundary-Layer Interactions at Mach 8.3. Technical Report NASA TM 103909, NASA Ames Research Center, Feb 1992.

[39] C. Becht and D. Knight. A Simple Low Reynolds Number Modification for the Compressible $k-\epsilon$ Model. Part I. Boundary Layer Flows. AIAA Paper 95-2218, 1995.

[40] G. Alexopoulos and H. Hassan. Computation of Crossing Shock Flows Using the k-enstrophy Turbulence Model. AIAA Paper No. 97-0206, 1997.

[41] K.-Y. Chien. Predictions of Channel and Boundary Layer Flows with a Low Reynolds Number Turbulence Model. *AIAA Journal*, 20:33–38, January 1982.

[42] B. Sekar. Three Dimensional Computations of Parallel and Non-Parallel Injection in Supersonic Flow. AIAA Paper No. 95-0886, 1995.

[43] G. Zha and D. Knight. Three-Dimensional Shock / Boundary-Layer Interaction Using Reynolds Stress Equation Turbulence Model. *AIAA Journal*, 34:1313–1320, July 1996.

[44] G. Zha, D. Smith, M. Schwabacher, A. Gelsey, and D. Knight. High performance supersonic missile inlet design using automated optimization. AIAA Paper No. 96-4142, 1996.

[45] M. Gnedin. *Numerical Simulation of 3-D Shock Wave Turbulent Boundary Layer Interaction Using a Two Equation Model of Turbulence*. PhD thesis, Rutgers University, May 1996.

[46] M. Gnedin, D. Knight, A. Zheltovodov, A. Maksimov, A. Shevchenko, and S. Vorontsov. 3-D Crossing Shock Wave Turbulent Boundary Laer Interaction. AIAA Paper No. 96-2001, 1996.

[47] P. Roe. Approximate Riemann Solvers, Parameter Vectors, and Difference Schemes. *Journal of Computational Physics*, 43:357–372, 1981.

[48] D. Dolling. Problems in the Validation of CFD Codes through Comparison with Experiment. AGARD Symposium on Theoretical and Experimental Methods in Hypersonic Flows, Turin, Italy, 1992.

[49] T. Garrison, G. Settles, N. Narayanswami, and D. Knight. Comparison of Flowfield Surveys and Computations of a Crossing - Shock Wave / Boundary - Layer Interaction. AIAA Paper 94-2273, June 1994.

[50] W. L. Hankey and M. S. Holden. Two-dimensional shock wave-boundary layer interactions in high speed flows. AGARDograph 203, 1975.

[51] B. Chanetz. Study of an axisymmetric shock wave/boundary layer interaction in hypersonic laminar flow. TR 42/4362 AN, ONERA, 1995.

[52] A. Joulot. *Contribution à l'étude de l'interaction onde de choc-couche limite sur rampe bidimensionnelle en régime hypersonique*. PhD thesis, Université Pierre et Marie Curie, Paris, 1992.

[53] E. Issman, G. Degrez, and H. Deconinck. Implicit upwind residual-distribution Euler and Navier-Stokes solver on unstructured meshes. *AIAA Journal*, 34(10):2021–2029, 1996.

[54] J. N. Moss, V. K. Dogra, and J. M. Price. DSMC simulations of viscous interactions for a hollow cylinder-flare configuration. AIAA Paper 94-2015.

[55] B. Chanetz, R. Benay, J.-M. Bousquet, R. Bur, T. Pot, F. Grasso, and J. Moss. Experimental and Numerical Study of the Laminar Separation in Hypersonic Flow. *Aerospace Science and Technology*, 1997. to be published.

[56] P. R. Spalart and S. R. Allmaras. A one-equation turbulence model for aerodynamic flows. *La Recherche Aérospatiale*, (1):5–21, 1994.

[57] R. Paciorri, H. Deconinck, and G. Degrez. Implementation and validation of the Spalart-Allmaras turbulence model for application in hypersonic flows. Technical Note 190, von Karman Institute, 1996.

[58] G. Inger. Supersonic Viscous-Inviscid Interaction of a Swept Ramp with a Turbulent Boundary Layer. AIAA Paper 85-1669, 1985.

[59] G. Inger. Incipient Separation and Similitude Properties of Swept Shock/Turbulent Boundary Layer Interactions. AIAA Paper 86-0345, 1986.

[60] G. Inger. Spanwise Propagation of Upstream Influence in Conical Swept Shock / Boundary Layer Interactions. *AIAA Journal*, 25:287–293, 1987.

[61] K. Stewartson. Some Recent Studies in Triple-Deck Theory. In T. Cebeci, editor, *Numerical and Physical Aspects of Aerodynamic Flows*, page 142. Springer-Verlag, 1981.

[62] A. Borisov, A. Zheltovodov, A. Maksimov, N. Fedorova, and S. Shpak. Verification of Turbulence Models and Computational Methods of Supersonic Separated Flows. In *Proceedings of the International Conference on Methods of Aerophysical Research*, pages 54–61, September 1996. Russian Academy of Sciences, Siberian Division.

[63] I. Bedarev, A. Zheltovodov, and N. Fedorova. Supersonic Turbulent Separated Flows Numerical Model Verification. In *Proceedings of the International Conference on Methods of Aerophysical Research*, pages 30–35, June 1998. Russian Academy of Sciences, Siberian Division.

[64] D. C. Wilcox. *Turbulence Modelling for CFD*. DCW Industries, 1993.

[65] D. Dolling. Unsteady Phenomena in Shock - Wave / Boundary Layer Interaction. In *AGARD/VKI Special Course on Shock-Wave Boundary-Layer Interactions in Supersonic and Hypersonic Flows*, pages 4–1 to 4–46. Von Karman Institute for Fluid Dynamics, May 1993. AGARD R-792.

[66] F. Alvi and G. Settles. Structure of Swept Shock Wave / Boundary Layer Interactions Using Conical Shadowgraphy. AIAA Paper 90-1644, 1990.

[67] R. Courant and K. Friedrichs. *Supersonic Flow and Shock Waves*. Springer-Verlag, New York, 1948.
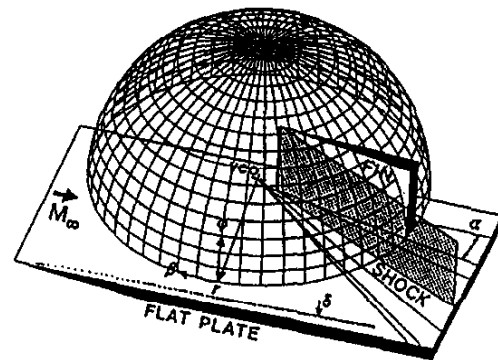
A Conical Flow

Figure 113: Spherical polar coordinates (from [66])

A conical flow is a steady flowfield whose Cartesian velocity components u_i, static pressure p and static temperature T are invariant with radial distance from a common vertex [67]. Consider the spherical polar coordinate system (R, β, ϕ) shown in Fig. 113. Thus,

$$\frac{\partial u_i}{\partial R} = 0$$

$$\frac{\partial p}{\partial R} = 0$$

$$\frac{\partial T}{\partial R} = 0$$

where R is the spherical polar radius

$$R = \sqrt{(x-x_0)^2 + (y-y_0)^2 + (z-z_0)^2}$$

where (x_0, y_0, z_0) is the Virtual Conical Origin. For the single fin, the VCO is close to the intersection of the fin with the flat plate. The velocity, pressure and temperature are functions of the spherical polar coordinates

$$\beta = \tan^{-1}\left((z-z_0)/(x-x_0)\right)$$
$$\phi = \tan^{-1}\left((y-y_0)/\sqrt{(x-x_0)^2 + (z-z_0)^2}\right)$$